# RESEARCH ARTICLE

**Key Points:**
- For the first time, long-term data sets are used to study the summer and winter season RSD
- RSDs differ considerably between summer and winter rainfall and type of precipitation
- Dynamical and thermodynamical interactions are found to impact the RSD variations between summer and winter rainfall

**Author Contributions:**
**Conceptualization:** Balaji Kumar Seela, Jayalakshmi Janapati, Pay-Liam Lin, Pao K. Wang
**Data curation:** Pay-Liam Lin
**Formal analysis:** Balaji Kumar Seela, Jayalakshmi Janapati, Meng-Tze Lee
**Funding acquisition:** Pay-Liam Lin
**Investigation:** Balaji Kumar Seela, Jayalakshmi Janapati, Pay-Liam Lin
**Methodology:** Balaji Kumar Seela, Jayalakshmi Janapati, Pay-Liam Lin
**Resources:** Pay-Liam Lin
**Supervision:** Pay-Liam Lin, Pao K. Wang
**Validation:** Balaji Kumar Seela, Jayalakshmi Janapati, Pay-Liam Lin
**Visualization:** Jayalakshmi Janapati, Meng-Tze Lee
**Writing - original draft:** Balaji Kumar Seela, Jayalakshmi Janapati
**Writing – review & editing:** Balaji Kumar Seela, Jayalakshmi Janapati, Pay-Liam Lin, Pao K. Wang

# Raindrop Size Distribution Characteristics of Summer and Winter Season Rainfall Over North Taiwan

**Balaji Kumar Seela**[1,2] (ID), **Jayalakshmi Janapati**[1] (ID), **Pay-Liam Lin**[1,3] (ID), **Pao K. Wang**[4,5], and **Meng-Tze Lee**[1]

[1]Institute of Atmospheric Physics, Department of Atmospheric Sciences, National Central University, Taoyuan City, Taiwan, [2]Taiwan International Graduate Program, Earth System Science Program, Research Center for Environmental Changes, Academia Sinica, Taipei, Taiwan, [3]Earthquake-Disaster and Risk Evaluation and Management Center, National Central University, Taoyuan City, Taiwan, [4]Department of Atmospheric and Oceanic Sciences, University of Wisconsin-Madison, Madison, WI, USA, [5]Research Center for Environmental Changes, Academia Sinica, Taipei, Taiwan

**Abstract** Raindrop size distribution (RSD) characteristics of summer and winter seasons over north Taiwan are analyzed by using long-term (~12 years) raindrop spectra from Joss-Waldvogel disdrometer located at National Central University (24°58′N, 121°10′E), Taiwan. Along with the disdrometer data, radar reflectivity mosaic from six ground-based radars, Tropical Rainfall Measuring Mission, Moderate Resolution Imaging Spectroradiometer, and ERA-Interim data sets are used to establish the dynamical and microphysical characteristics of summer and winter rainfall. Significant differences in raindrop spectra of summer and winter rainfall are noticed. Winter rainfall has a higher concentration of small drops and a lower concentration of midsize and large drops when compared to summer rainfall. RSD stratified on the basis of rain rate showed a higher mass-weighted mean diameter ($D_m$) and a lower normalized intercept parameter ($\log_{10}N_w$) in summer than winter. Similarly, diurnal variation of RSD showed higher $D_m$ and lower $\log_{10}N_w$ values in summer as compared to winter rainfall. In addition, for both seasons, the mean value of $D_m$ is higher in convective precipitation than stratiform. Radar reflectivity ($Z$) and rain rate ($R$) relations ($Z = A*R^b$) showed a clear demarcation between summer and winter rainfall. Higher ground temperatures, deeply extended clouds with intense convective activity in summer modified the RSD through evaporation, drop sorting, and collision-coalescence processes resulting with higher $D_m$ and lower $\log_{10}N_w$ values in summer as compared to winter rainfall.

**Plain Language Summary** This study details about the raindrop size distribution characteristics variations between summer and winter seasons of north Taiwan using long-term (12 years) disdrometer data and the possible reasons for the raindrop size distribution variations are also detailed.

## 1. Introduction

Knowledge about the raindrop size distribution (RSD) is useful in realizing rain integral parameters and in understanding of precipitation microphysics (Rosenfeld & Ulbrich, 2003). RSD study establishes quantitative precipitation estimation (QPE) algorithms for radar measurements through radar reflectivity ($Z$) and rain rate ($R$) relations ($Z = A*R^b$, Boodoo et al., 2015; Ryzhkov & Zrnic, 1995; Seliga & Bringi, 1976) and plays a significant role in improving microphysical parameterization in modeling studies (Cohen & McCaul, 2006; Fadnavis et al., 2014; Gilmore et al., 2004; McFarquhar et al., 2015; Tapiador et al., 2014; Wainwright et al., 2014). Rain integral parameters deduced from RSD are helpful in soil erosion studies (Angulo-Martinez & Barros, 2015; Nanko et al., 2016; Rosewell, 1986) and also in understanding of runoff process and flood hazards control (Smith et al., 2009). Specific attenuation of electromagnetic waves proceeding through rain is dependent on the RSD; as a result, RSD characteristics and their variability play a vital role in terrestrial and earth to space radio links operating at frequencies above 10 GHz (Badron et al., 2011; Chakravarty & Maitra, 2010; Kumar et al., 2010; Marzuki et al., 2009). Modeled RSD parameters play a key role in active and passive satellite-based microwave sensor rainfall estimation. For instance, three-parameter gamma distribution has been used in the rainfall estimation algorithms of Tropical Rainfall Measuring Mission (TRMM) precipitation radar (PR; Iguchi et al., 2000; Kozu, Iguchi, et al., 2009; Kozu, Shimomai, & Kashiwagi, 2009) and in Global Precipitation Measurement Dual-frequency Precipitation Radar (Hou et al., 2008; Liao et al., 2014; Nakamura & Iguchi, 2007).

RSD characteristics were found to vary with rainfall type, geographical location, storm to storm, within a storm, and season to season (Janapati et al., 2017; Kumar & Reddy, 2013; Kumari et al., 2014; Seela et al., 2017; Tokay & Short, 1996). Over Asia region an adequate research was carried on seasonal RSD features. For example, Kozu et al. (2006) demonstrated the seasonal and diurnal RSD variations of three different locations over Asia region (Gadanki, Singapore, and Kototabang). They conceived predominant seasonal dissimilarity over inland station (Gadanki), most significant diurnal variation over maritime continental station (Kototabang), and less seasonal and diurnal variation over Singapore. Over India, seasonal exploration of RSD revealed distinct variations from southwest monsoon to northeast monsoon (Jayalakshmi & Reddy, 2014; Rao et al., 2009; Reddy & Kozu, 2003), and monsoon months to that of premonsoon and postmonsoon months (Chakravarty et al., 2013; Chakravarty & Raj, 2013; Sreekanth et al., 2017). Over the maritime continental station (Sumatra), Marzuki et al. (2013) perceived higher mass-weighted mean diameter ($D_m$) values in northeast monsoon (December–March) than southwest monsoon (June–September). They also reported unlike $Z$-$R$ relations for the three rainfall types (stratiform, deep convection, and shallow convection) of three (presouthwest: April–May, southwest, and northeast) monsoon seasons. Suh et al. (2016) examined the climatological RSD characteristics for Busan, Republic of Korea, a complex midlatitude region. They found noteworthy seasonal and diurnal variations in RSD characteristics. RSD variations in easterly and westerly monsoon wind regimes of an oceanic station at Palau islands were inspected by Krishna et al. (2016), and they revealed profound differences in microphysical characteristics between these two seasons. Nonetheless, most of the previous seasonal RSD studies over Asia region have been carried out for inland or coastal stations and very few over the oceanic region (Krishna et al., 2016). In western North Pacific, especially over Taiwan, seasonal RSD investigations are yet to be documented particularly with long-term data.

Taiwan is a subtropical island located in the northwest Pacific separated from the southeastern coast of China. It has complex topography with its central mountain range extending almost in the north-south direction. Rainfall in Taiwan is mainly produced by the southwesterly (May–August) and northeasterly (September–April) monsoon season (Chen et al., 1999). On the basis of rainfall regimes, seasons over Taiwan are classified as winter, spring, mei-yu, summer, typhoon, and autumn (C. S. Chen & Chen, 2003; T.-C. Chen et al., 1999). The rainfall characteristics of different seasons and their synoptic situations of Taiwan were well detailed previously (C. S. Chen & Chen, 2003; T.-C. Chen et al., 1999). Nevertheless, the rain microphysical characteristics of this island are less studied. It is important to report the rain integral parameters and their relations for a given location in establishing quantitative precipitation forecast and modeling studies. Though there were few case studies on tropical cyclones (W.-Y. Chang, Wang, & Lin, 2009), squall line (Jung et al., 2012), or combination of different weather systems (Chu & Su, 2008) for this region, so far, there were no seasonal RSD studies especially using long-term raindrop measurements. Tokay et al. (2013) pointed out that long-term observations of disdrometer can provide robust features of RSD parameters and are helpful in eliminating the assumptions of constant shape parameter in ground-based radar and Global Precipitation Measurement Dual-frequency Precipitation Radar algorithms (Brandes et al., 2002; Kozu, Shimomai, & Kashiwagi, 2009; Vivekanandan et al., 2004). This motivated us to carry out the present study with principal objectives: Are there any seasonal RSD differences between summer and winter for the western Pacific island, Taiwan, and if they exit, what could be the conceivable mechanisms for the differences. Are the drop size parameters of Taiwan show similar/dissimilar characteristics to the previous studies? Can we continue the usage of currently adopting $Z$-$R$ relations in Taiwan QPE, or do we need to revise them? Henceforth, in this study, we report the RSD characteristics of summer and winter season rainfall and for the type of precipitation (stratiform and convective) by using data from Joss-Waldvogel disdrometer (JWD) installed at National Central University (NCU; 24°58′N, 121°10′E, 130 above sea level) in north Taiwan. Summer and winter rainfall are separated into stratiform and convective type by adopting Bringi et al. (2003) method. As Bringi et al. (2003) established a range of $D_m$ and $\log_{10}N_w$ values for the maritime and continental cluster with the RSD measurements for a wide range of locations, we adopted their classification criteria to compare the current results with their cluster type.

Following this introduction, a brief explanation of data and methodology used in the present study is provided in section 2. RSD variations of summer and winter rainfall are detailed in section 3 and followed by section 4, which includes the possible reasons for the RSD variations in summer and winter seasons. Conclusions drawn from the observational results are provided in section 5.
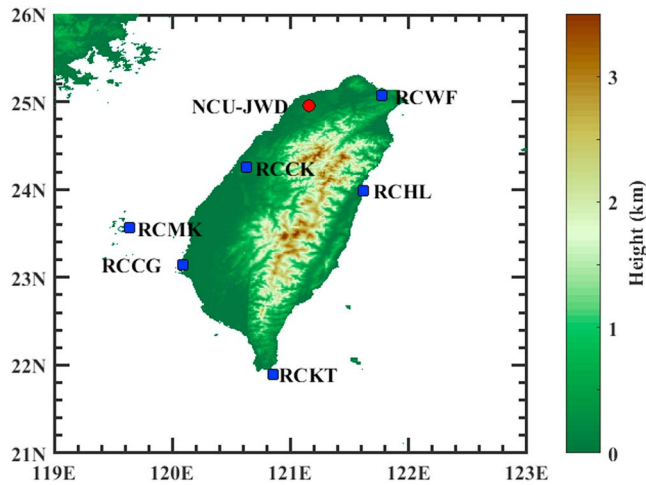
**Figure 1.** Geographical location of Taiwan. The red-colored circle represents the location of National Central University-Joss-Waldvogel disdrometer (NCU-JWD), and the locations of radar sites are represented with blue squares.

## 2. Data and Methodology

### 2.1. JWD Data

In the current study, data collected from JWD installed at NCU (24° 58′N, 121° 10′E) located in north Taiwan are utilized. The geographical location of the NCU JWD is shown with the red-colored circle in Figure 1. The location of the radar observational sites (blue-colored squares) can also be seen in this figure (Figure 1). The data recorded by the JWD (for every 60 s) span from the year 2002 to 2016 and are not available for the winter season of the year 2003 and summer season of years 2003, 2008, and 2009. As the RSD characteristics of tropical cyclones were found to be different from that of the seasonal rainfall (Deo & Walsh, 2016; Kumar & Reddy, 2013; Radhakrishna & Rao, 2010), the RSD measurements during typhoon periods are not considered in the present study. To identify snowfall occurrence, S. Chen, Hong, et al. (2016) used the surface temperatures threshold criteria; that is, if the environment on the surface that temperature <2 °C and wet-bulb temperature <2 °C, the particles observed on surface can be assumed as snowfall particles. Similar temperature threshold applied to the present observational site showed (from Table 1) no snowfall occurrence during the winter seasons of the considered years. Further, to endorse that there were no hailstorm occurrences in the summer seasons, a hail identification parameter (vertical integrated liquid density, VILD) adopted by J. Zhang et al. (2009) from Amburn and Wolf (1997) is used in the present study. The VILD values listed for the summer seasons in Table 1 reveal that (VILDs <2 g/m$^3$) there were no hail occurrences over the observational site.

The JWD is an impact-type disdrometer consisting of styrofoam cone of cross-sectional area 50 cm$^2$ (Joss & Waldvogel, 1969). It can measure raindrops of size ranging from 0.3 to 5.3 mm with an accuracy of 5%. Once a raindrop hits the surface of the disdrometer, the styrofoam transmits the mechanical impulse of the hitting drop to a two moving coil setup in magnetic fields, and this will induce voltage in the sensing coil. The induced voltage is amplified in the sensor head and transmitted to secondary coil. In the secondary coil, electromagnetic force is produced to restore the sensing body to the rest position. The amplitude of output pulse at the amplifier is a measure of the raindrop size. Raindrops of different sizes (0.3 to 5.3 mm) are

**Table 1**
*Minimum, Maximum, Mean Values of Daily Mean Ground Temperatures at JWD Observational Site for Winter Seasons, and VILD for Summer Seasons From 2002 to 2016*

| | Winter | | | | | | Summer | | |
|---|---|---|---|---|---|---|---|---|---|
| | Air temperature (°C) | | | Dew point temperature (°C) | | | VILD (g/m$^3$) | | |
| Year | Minimum | Maximum | Mean | Minimum | Maximum | Mean | Minimum | Maximum | Mean |
| 2002 | 10.95 | 19.13 | 15.31 | 9.52 | 17.97 | 13.83 | [a] | [a] | [a] |
| 2003 | [b] | [b] | [b] | [b] | [b] | [b] | [a] | [a] | [a] |
| 2004 | 7.12 | 20.69 | 15.49 | 2.52 | 16.97 | 11.01 | [a] | [a] | [a] |
| 2005 | 5.99 | 20.69 | 15.01 | 2.52 | 18 | 11.49 | 0.026 | 0.488 | 0.166 |
| 2006 | 7.63 | 21.34 | 15.45 | 2.52 | 18 | 11.86 | 0.002 | 0.319 | 0.095 |
| 2007 | 10.52 | 20.69 | 15.92 | 2.52 | 18 | 12.53 | 0.015 | 0.497 | 0.202 |
| 2008 | 7.91 | 20.69 | 14.71 | 2.52 | 16.98 | 11.69 | [b] | [b] | [b] |
| 2009 | 7.91 | 20.69 | 15.23 | 2.52 | 17 | 11.85 | [b] | [b] | [b] |
| 2010 | 8.14 | 20.69 | 14.98 | 2.52 | 16.98 | 11.56 | 0.056 | 0.711 | 0.324 |
| 2011 | 8.13 | 22.39 | 14.94 | 2.52 | 18.78 | 11.4 | 0.009 | 1.753 | 0.400 |
| 2012 | 8.38 | 20.69 | 15 | 2.52 | 18.46 | 11.83 | 0.003 | 0.387 | 0.141 |
| 2013 | 10.16 | 21.61 | 15.55 | 2.52 | 18.39 | 12.27 | 0.033 | 0.758 | 0.165 |
| 2014 | 6.68 | 20.69 | 14.89 | 2.52 | 17.34 | 11.41 | 0.006 | 0.262 | 0.105 |
| 2015 | 10.12 | 20.69 | 15.71 | 2.52 | 17.83 | 12.15 | [a] | [a] | [a] |
| 2016 | 6.16 | 21.38 | 15.54 | 2.52 | 19.4 | 12.19 | [a] | [a] | [a] |

*Note.* VILD = vertical integrated liquid density.
[a]No radar data.   [b]No disdrometer data.

**Table 2**
*Joss-Waldvogel Disdrometer Channel Parameters*

| Channel no. (i) | Mean diameter of drops in channel i, $D_i$ (mm) | Diameter interval of drop size channel i, $\Delta D_i$ (mm) | Fall velocity of a drop with diameter $D_i$, V ($D_i$; m/s) |
|---|---|---|---|
| 1 | 0.359 | 0.092 | 1.435 |
| 2 | 0.455 | 0.100 | 1.862 |
| 3 | 0.551 | 0.091 | 2.267 |
| 4 | 0.659 | 0.119 | 2.692 |
| 5 | 0.771 | 0.112 | 3.154 |
| 6 | 0.913 | 0.172 | 3.717 |
| 7 | 1.116 | 0.233 | 4.382 |
| 8 | 1.331 | 0.197 | 4.986 |
| 9 | 1.506 | 0.153 | 5.423 |
| 10 | 1.665 | 0.166 | 5.793 |
| 11 | 1.912 | 0.329 | 6.315 |
| 12 | 2.259 | 0.364 | 7.009 |
| 13 | 2.584 | 0.286 | 7.546 |
| 14 | 2.869 | 0.284 | 7.903 |
| 15 | 3.198 | 0.374 | 8.258 |
| 16 | 3.544 | 0.319 | 8.556 |
| 17 | 3.916 | 0.432 | 8.784 |
| 18 | 4.350 | 0.446 | 8.965 |
| 19 | 4.859 | 0.572 | 9.076 |
| 20 | 5.373 | 0.455 | 9.137 |

separated into 20 size bins and intervals of each channel increases with drop size from 0.1 to 0.5 mm (Table 2). The JWD can directly estimate the rain integral parameters like rain rate, radar reflectivity, and liquid water content. The pros and cons of the JWD have been discussed by many researchers (Cao et al., 2008; Joss & Waldvogel, 1969; Lee & Zawadzki, 2005; McFarquhar & List, 1993; Sauvageot & Lacaux, 1995; Sheppard, 1990; Sheppard & Joe, 1994; Tokay et al., 2001; see also http://www.distromet.com). In heavy rain, if two or more drops strike the styrofoam of the disdrometer at the same time, the small drops will be undercounted because of registration of largest drops in these instances and are called as dead time of the disdrometer. The undercounted small drops can be corrected by using equation 2 of Sheppard and Joe (1994). This dead time correction does not increase the counts when the channel has no drops (Tokay & Short, 1996). Moreover, as mentioned by Tokay and Short (1996), the derived relationships would have less than 3% effect from the underestimated small drops. Hence, in the present study, standard output of the JWD is used without any dead time correction. In order to reduce the sampling errors due to insufficient raw drop counts (<10 drops), rain rates less than 0.1 mm/hr are not used in the current analysis (Tokay & Short, 1996).

The raindrop concentration $N(D)$ (m$^{-3}$ mm$^{-1}$) at an instant of time from JWD is obtained from the following equation:

$$N(D) = \Sigma_{i=1}^{20} \frac{n_i}{A \times \Delta t \times v_{(D_i)} \times \Delta D_i} \qquad (1)$$

where $n_i$ is the number of drops reckoned in the size bin i, $A$ (m$^2$), and $\Delta t$ (s) are the sampling area and time, $D_i$ (mm) is the drop diameter for the size bin i and $\Delta D_i$ is the corresponding diameter interval (mm), $v(D_i)$ (m/s) is terminal velocity of the raindrops in $i$th channel and is estimated from $v(D_i) = 9.65 - 10.3 \times \exp(-0.6 \times D_i)$ (Gunn & Kinzer, 1949). Further, the raindrop concentration, $N(D)$, of summer and winter rainfall is computed by using the fall velocity equations of Gunn and Kinzer (1949) and Campos et al. (2006) for 12 years of data. The $N(D)$ computed with the said terminal velocity equations showed no much difference for both summer and winter rainfall.

From the raindrop concentration $N(D)$, drop diameter ($D_i$), and terminal velocity V ($D_i$), radar reflectivity factor $Z$ (mm$^6$/m$^3$) and rain rate $R$ (mm/hr) are derived by using the equation:

$$Z = \Sigma_{i=1}^{20} N(D_i) D_i^6 \Delta D_i \qquad (2)$$

$$R = 6\pi \times 10^{-4} \Sigma_{i=1}^{20} V(D_i)\, N(D_i) D_i^3 \Delta D_i \qquad (3)$$

Validation of JWD is done by comparing the daily accumulated precipitation of JWD with the collocated tipping bucket rain gauge of automatic weather station (AWS). In addition to rainfall measurements, AWS can record surface meteorological parameters (pressure, temperature, and relative humidity) at 1-min sampling interval. The tipping bucket rain gauge can measure a minimum rainfall amount of 0.5 mm. The scatter plots of JWD and AWS daily accumulated rainfall for summer and winter seasons are given in Figure 2. Two summer events in Figure 2a show AWS values around 65 mm, while the JWD values around 45 mm. The discrepancy between AWS and JWD measurements for these two outlier could be due to the following reasons. As the maximum measurable size of the JWD is 5.4 mm, any drops larger than 5.4 mm would be counted in the largest size bin and this will result in underestimation of rain rate in heavy rain events. Recording of zero drops in first three to four channels during dead time of the disdrometer in two heavy rainfall events of summer (two outliers in Figure 2a) could be the other possible reason for the difference between AWS and disdrometer measurements (Tokay & Short, 1996). The linear fits applied to the scatter plots of summer and winter season rainfall show higher correlation coefficients between the JWD and AWS measurements. This clearly suggests that the rain integral parameters derived from the JWD can be utilized to understand the
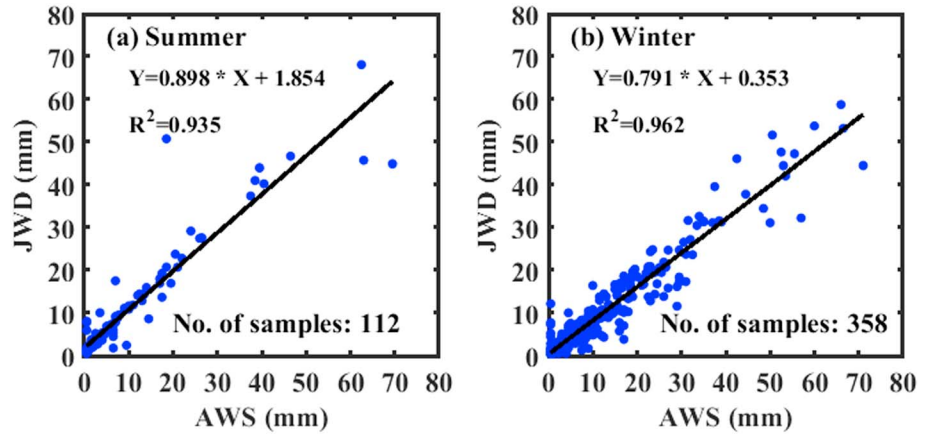
**Figure 2.** (a, b) Scatter plot between daily accumulated rainfall of Joss-Waldvogel disdrometer (JWD) and the collocated tipping bucket rain gauge of the automatic weather station (AWS).

summer and winter rainfall RSD characteristics of north Taiwan. The 1-min RSD data sets are fitted with gamma function from Ulbrich (1983). The functional form of the gamma distribution is given as

$$N(D) = N_0 D^\mu \exp(-\Lambda, D) \tag{4}$$

where $D$ (mm) is the drop diameter, $N(D)$ ($m^{-3}$ $mm^{-1}$) is number of drops per unit volume per unit size interval, $N_0$ ($m^{-3}$ $mm^{-1}$) is number concentration parameter, $\mu$ (−) is shape parameter, and $\Lambda$ ($mm^{-1}$) is slope parameter.

The slope parameter, $\Lambda$ ($mm^{-1}$), is given by

$$\Lambda = \frac{(\mu + 4)M_3}{M_4} \tag{5}$$

where $\mu$ is the shape parameter without dimensions and is given by

$$\mu = \frac{(11G - 8) + \sqrt{G(G + 8)}}{2(1 - G)} \tag{6}$$

where

$$G = \frac{M_4^3}{M_6 M_3^2} \tag{7}$$

The normalized intercept parameter $N_w$ ($m^{-3}$ $mm^{-1}$) is defined by Bringi et al. (2003) as

$$N_w = \frac{4^4}{\pi \rho_w} \left( \frac{W}{D_m^4} \right) \tag{8}$$

where $\rho_w$ ($10^{-3}$ $g/mm^3$) represents the density of water and $W$ ($g/m3$) represents the liquid water content for the corresponding size distribution and can be calculated by using the following equation.

$$W = \frac{\pi}{6} \times \rho_w \Sigma_{i=1}^{20} N(D_i) D_i^3 \Delta D_i \tag{9}$$

The $n$th-order moment of the drop size distribution is expressed as

$$M_n = \int_{D_{min}}^{D_{max}} D^n N(D) dD \tag{10}$$

Here $n$ stands for the $n$th moment of the size distribution.

The mass-weighted mean diameter $D_m$, shape parameter $\mu$, and slope parameter $\Lambda$ are evaluated from the third, fourth, and sixth moments of the size distribution.

$$D_m = \frac{M_4}{M_3} \tag{11}$$

The normalized intercept parameter $N_w$ represents $N(D)$ when raindrop diameter approaches to its minimum value. The slope parameter ($\Lambda$) designates the truncation of RSD tail with drop diameter. A smaller value of $\Lambda$ indicates the extension of RSD tail to a larger diameter and larger $\Lambda$ to a smaller diameter. The shape ($\mu$) parameter represents the breadth of RSD. If $\mu$ is greater than 0, then RSD is concave downward, concave upward if $\mu$ is less than 0, and is exponential if it is equal to 0 (Ulbrich, 1983).

The percentage parameter of $N(D)$ for different rain rate class, $\delta(D, R) = \delta(D, R_{Ck})_{summer/winter}$ is given as

$$\delta(D, R_{Ck})_{summer} = \frac{\left[N(D)_{summer}\right]_{Ck}}{\left(\left[N(D)_{summer}\right]_{Ck} + \left[N(D)_{winter}\right]_{Ck}\right)} \times 100 \tag{12}$$

$$\delta(D, R_{Ck})_{winter} = \frac{\left[N(D)_{winter}\right]_{Ck}}{\left(\left[N(D)_{summer}\right]_{Ck} + \left[N(D)_{winter}\right]_{Ck}\right)} \times 100 \tag{13}$$

where $[N(D)_{summer}]_{Ck}$ or $[N(D)_{winter}]_{Ck}$ represents the mean $N(D)$ of summer or winter rainfall for the rain rate class $Ck$, with $k = 1, 2, 3, 4, 5, 6$ (C1: $0.1 \leq R < 1$, C2: $1 \leq R < 2$, C3: $2 \leq R < 5$, C4 $= 5 \leq R < 10$, C5 $= 10 \leq R < 20$, and C6 $= R \geq 20$ mm/hr).

The percentage parameter of $N(D)$ for 3-hourly rainfall, $\delta(D, T) = \delta(D, T_h)_{summer/winter}$ is given as

$$\delta(D, T_h)_{summer} = \frac{\left[N(D)_{summer}\right]_h}{\left(\left[N(D)_{summer}\right]_h + \left[N(D)_{winter}\right]_h\right)} \times 100 \tag{14}$$

$$\delta(D, T_h)_{winter} = \frac{\left[N(D)_{winter}\right]_h}{\left(\left[N(D)_{summer}\right]_h + \left[N(D)_{winter}\right]_h\right)} \times 100 \tag{15}$$

where $[N(D)_{summer}]_h$ or $[N(D)_{winter}]_h$ represents mean $N(D)$ of summer or winter rainfall for 3-hourly rainfall (h) with $h = 00–03, 03–06, 06–09, 09–12, 12–15, 15–18, 18–21$, and $21–24$ hr local time.

In computing the reflectivity-rain rate (Z-R) relations, a linear regression is applied to $10\log Z$ and $\log R$ for summer and winter season rainfall and for the type of rainfall (stratiform and convective).

### 2.2. Radar Data

To elucidate the winter and summer rainfall characteristics, radar reflectivity mosaic obtained from six ground-based radars installed over Taiwan (shown with blue-colored squares in Figure 1) is used. Among six radars, four Doppler radars of Central Weather Bureau are installed at Wu-Fan San (RCWF: 121.77°E, 25.07°N), Hual-Lien (RCHL: 121.619°E, 23.989°N), Chi-Gu (RCCG: 120.086°E, 23.1467°N), and Ken-Ting (RCKT: 120.849°E, 21.899°N). All these four radars have a beam width of 1° and wavelength of 10 cm (S-band). Further details of these radars can be found in P.-L. Chang, Lin, et al. (2009). Remaining two radars (C-band dual polarimetric) of Taiwan air force are located at Ma-Kung (RCMK: 119.634°E, 23.563°N) and Ching-Chuan-Kang (RCCK: 120.63°E, 24.25°N). RCMK radar has scanning time interval of 7.5 min, and the Nyquist velocity of 37.18 m/s. The maximum observation range of RCCK radar is 150 km, and the Nyquist velocity is 37.5 m/s. The radar reflectivity mosaic of six radars is archived by Central Weather Bureau and is available at a spatial resolution of 0.0125° on the latitude-longitude coordinate system and at a 10-min update cycle (J. Zhang et al., 2005, 2009). In the present study radar reflectivity mosaic available from 2005 to 2014 are used over JWD observational site (24.55°N $-$24.6°N, 121.0875°E $-$121.1375°E).

### 2.3. Satellite and ERA-Interim Data

In addition to ground-based instruments, TRMM, Moderate Resolution Imaging Spectroradiometer (MODIS), and European Centre for Medium-Range Weather Forecasts Interim Re-Analysis (ERA-Interim), data sets over north Taiwan (24°–25.2°N and 121°–121.9°E) are used. Storm top heights and bright band
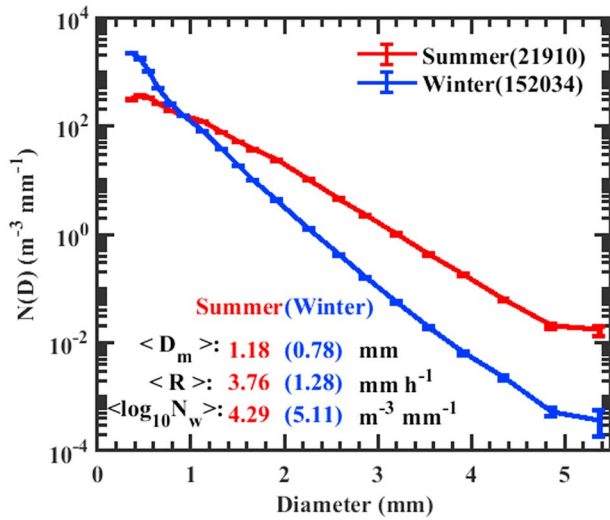
**Figure 3.** Variation of mean raindrop concentration, $N(D)$ (m$^{-3}$ mm$^{-1}$) with drop diameter, D (mm) for summer and winter rainfall. The numbers in the legend parenthesis indicate the total number of samples in summer and winter rainfall. The mean raindrop size distribution parameters (represented with angles brackets < >) of summer and winter rainfall are also shown in the figure. The error bars represents the standard error of each channel samples.

heights (BBHs) are obtained from the TRMM PR 2A23 data product. The 2A23 data product provides storm, freezing, and BBHs from PR (13.8 GHz) at 4.3-/5-km horizontal resolution over a 215-/247-km swath during preboost (before 7 August 2001)/postboost (after 24 August 2001) covering the tropical region from 37°S to 37°N. The data description and algorithm for level 2A23 data are available in TRMM PR algorithm instruction manual for version 7, and the further details can be seen in Awaka et al. (1997, 2009), Iguchi et al. (2000), and Kummerow et al. (2001). In addition to this, mean cloud effective radius (CER, μm) of ice and water droplets from MODIS level 3 data product (Platnick et al., 2015) are used. Level 3 daily data product (MOD08_D3) of MODIS consists of 1° × 1° grid average values of atmospheric parameters related to aerosol particle properties, water vapor, and cloud optical and physical properties (Remer et al., 2005). Bispectral solar reflectance method described by Nakajima and King (1990) was used for the retrieval of cloud effective radii from the MODIS satellite. Details about the MODIS cloud product algorithms are provided in Platnick et al. (2003) and King et al. (2003). Besides CER, the cloud droplet number concentration ([DNC [$N$, m$^{-3}$]) values for summer and winter seasons also derived by using two cloud parameters (CER [$r_{e,top}$, μm] retrieved from 3.7-μm band and cloud optical thickness [$\tau$,−]) from the MODIS level 3 data product. The CDNC is estimated by using equation 2 of Bennartz and Rausch (2017).

$$N = \frac{\tau^3}{k}[2W]^{-\frac{5}{2}}\left[\frac{3}{5}\pi Q\right]^{-3}\left[\frac{3}{4\pi\rho_l}\right]^{-2}\sqrt{C_w} \qquad (16)$$

where $W$ represents the liquid water path ($W = \frac{5}{9}\rho_l r_{e,top}$; Brenguier et al., 2000), $r_{e,top}$ is the CER at cloud top (retrieved from 3.7-μm band), $\rho_l$ (=10$^3$ kg/m$^3$) is the water density, $\tau$ is cloud optical thickness, $k$ (=0.8) is the dispersion of the assumed cloud droplet size distribution (Brenguier et al., 2011; Martin et al., 1994), $Q$ (=2) is the scattering efficiency of the cloud droplets, and $C_w$ (=2 × 10$^{-6}$ kg/m$^4$) is the condensation rate (Bennartz, 2007; Bennartz & Rausch, 2017; Pawlowska & Brenguier, 2003). In computing the CDNC, clouds with optical thickness less than 5 are removed in the present analysis (Zeng et al., 2014). Daily mean values of convective available potential energy (CAPE, J/kg) and vertical integral water vapor ($W$, kg/m$^2$) available at European Centre for Medium-Range Weather Forecasts ERA-Interim (Dee et al., 2011) with 0.125° × 0.125° grid resolution are used.

## 3. Observational Results

### 3.1. Seasonal Variation of RSD

A total number of 21,910 min of raindrop spectra in summer and 152,034 min of raindrop spectra in winter season were recorded by NCU JWD during the years 2002 to 2016 (excluding summer season of 2003, 2008, 2009 and winter season of 2003). Variations of mean raindrop concentration ($N(D)$, m$^{-3}$ mm$^{-1}$) with raindrop diameter (D, mm) for summer and winter seasons of the above-mentioned period are shown in Figure 3. In this work, by following the previous researchers' raindrop size classification, we considered raindrops below 1 mm as small drops, 1–3 mm as midsize drops, and above 3 mm as large drops (Jayalakshmi & Reddy, 2014; Krishna et al., 2016; Seela et al., 2017; Tokay et al., 2008). An inspection of raindrop spectra in Figure 3 shows that the raindrop concentration of small drops is higher in winter as compared to summer, and the number concentration of midsize and large drops is lower in winter than summer rainfall. The mean values of mass-weighted mean diameter ($D_m$), rain rate ($R$), and normalized intercept parameter ($\log_{10}N_w$) are given in Figure 3 as well. The mean values of $D_m$ and $R$ are higher in summer than winter, and the mean value of $\log_{10}N_w$ is lower in summer than winter. Relatively, a higher concentration of small drops and a lower concentration of midsize and large drops in winter are the possible reason for the lower mean $D_m$ value in winter than summer.
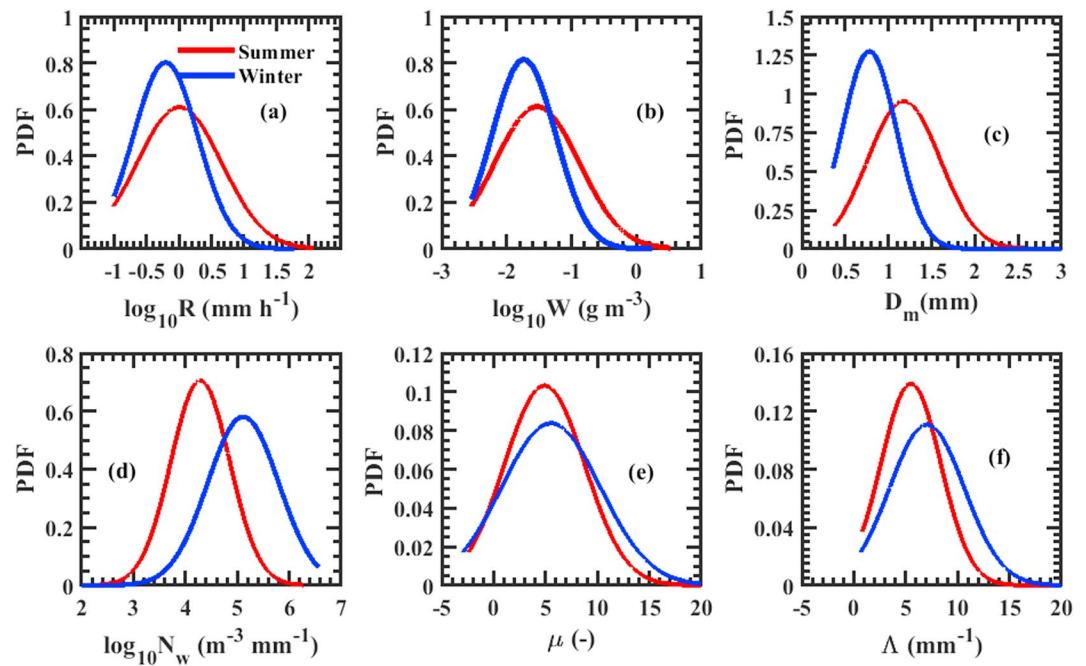
**Figure 4.** The probability distribution functions (PDFs) of (a) rain rate, $\log_{10}R$ (mm/hr), (b) liquid water content, $\log_{10}W$ (g/m$^3$), (c) mass-weighted mean diameter, $D_m$ (mm), (d) normalized intercept parameter, $\log_{10}N_w$ (m$^{-3}$ mm$^{-1}$), (e) shape parameter, $\mu$ ($-$), and (f) slope parameter, $\Lambda$ (mm$^{-1}$) for summer and winter rainfall.

**Table 3**
*Statistical Parameters of $\log_{10}R$, $\log_{10}W$, $D_m$, $\log_{10}N_w$, $\mu$ and $\Lambda$ for Summer and Winter Seasons and Student's t Test Results With Confidence Levels ($\alpha$) 0.05 and 0.01*

| Parameter | Rain rate, $\log_{10}R$ dB (mm/hr) | Liquid water content, $\log_{10}W$ dB (g/m$^3$) | Mass-weighted mean diameter, $D_m$ (mm) | Normalized intercept parameter, $\log_{10}N_w$ (m$^{-3}$ mm$^{-1}$) | Shape parameter, $\mu$ ($-$) | Slope parameter, $\Lambda$ (mm$^{-1}$) |
|---|---|---|---|---|---|---|
| | (summer) winter | (summer) winter | (summer) winter | (summer) winter | (summer) winter | (summer) winter |
| Mean | (3.76) 1.28 | (−1.53) −1.73 | (1.18) 0.78 | (4.29) 5.11 | (6.75) 12.29 | (10.89) 28.1 |
| Standard deviation | (9.23) 2.24 | (0.65) 0.49 | (0.42) 0.31 | (0.56) 0.69 | (8.59) 13.4 | (11.65) 32.13 |
| Skewness | (5.20) 6.84 | (0.60) 0.45 | (1.35) 1.16 | (−0.29) −0.46 | (5.18) 4.83 | (4.61) 6.23 |
| Kurtosis | (37.73) 88.36 | (2.76) 2.57 | (7.65) 5.31 | (3.45) 2.77 | (56.61) 141.81 | (36.15) 235.58 |
| Student t test (t Stat) | 39.57 | 39.41 | 136.01 | −196.43 | −82.03 | −151.06 |
| $P(T \le t)$ (one tail; $\alpha = 0.05$) | 0 | 0 | 0 | 0 | 0 | 0 |
| t critical (one tail; $\alpha = 0.05$) | 1.64 | 1.64 | 1.64 | 1.64 | 1.64 | 1.64 |
| $P(T \le t)$ (two tail; $\alpha = 0.05$) | 0 | 0 | 0 | 0 | 0 | 0 |
| t critical (two tail; $\alpha = 0.05$) | 1.96 | 1.96 | 1.96 | 1.96 | 1.96 | 1.96 |
| $P(T \le t)$ (one tail; $\alpha = 0.01$) | 0 | 0 | 0 | 0 | 0 | 0 |
| t critical (one tail; $\alpha = 0.01$) | 2.33 | 2.33 | 2.33 | 2.33 | 2.33 | 2.33 |
| $P(T \le t)$ (two tail; $\alpha = 0.01$) | 0 | 0 | 0 | 0 | 0 | 0 |
| t critical (two tail; $\alpha = 0.01$) | 2.58 | 2.58 | 2.58 | 2.58 | 2.58 | 2.58 |

**Table 4**
*Statistical Measure of Disdrometer-Derived Rain Rate Classes for Summer and Winter Rainfall of North Taiwan*

| Rain rate class | Rain rate threshold | Summer | | | | | Winter | | | | |
|---|---|---|---|---|---|---|---|---|---|---|---|
| | | No. of samples | Mean (mm/hr) | Standard deviation (mm/hr) | Skewness | Kurtosis | No. of data | Mean (mm/hr) | Standard deviation (mm/hr) | Skewness | Kurtosis |
| C1 | $0.1 \leq R < 1$ | 11,903 | 0.4 | 0.25 | 0.71 | 2.36 | 10,1019 | 0.39 | 0.25 | 0.77 | 2.49 |
| C2 | $1 \leq R < 2$ | 3,272 | 1.42 | 0.29 | 0.33 | 1.91 | 24,852 | 1.41 | 0.28 | 0.36 | 1.95 |
| C3 | $2 \leq R < 5$ | 3,381 | 3.17 | 0.84 | 0.46 | 2.08 | 19,368 | 3.08 | 0.82 | 0.61 | 2.29 |
| C4 | $5 \leq R < 10$ | 1,461 | 6.99 | 1.42 | 0.42 | 2 | 5,178 | 6.73 | 1.34 | 0.68 | 2.42 |
| C5 | $10 \leq R < 20$ | 871 | 14.23 | 2.9 | 0.29 | 1.88 | 1,317 | 13.09 | 2.59 | 0.87 | 2.79 |
| C6 | $R \geq 20$ | 1,022 | 38.76 | 18.2 | 1.57 | 5.58 | 300 | 28.6 | 8.45 | 1.46 | 4.8 |
| All classes | | 21,910 | 3.76 | 9.23 | 5.21 | 37.74 | 152,034 | 1.28 | 2.24 | 6.84 | 88.36 |

To find out the differences in rain integral parameters ($\log_{10}R$, $\log_{10}W$, $D_m$, $\log_{10}N_w$, $\mu$, and $\Lambda$) in summer and winter seasons, the probability distribution functions (PDFs) of these integral parameters are calculated and are given in Figure 4. The PDF distribution of rain rate shows that the peak frequency is higher for the winter distribution than for the summer distribution when $\log_{10}R < 0.2$ dB (mm/hr; Figure 4a). Similarly, the PDF of liquid water content ($\log_{10}W$) also shows a comparatively more frequency in winter compared to summer for $\log_{10}W < -1.3$ dB (g/m³; Figure 4b). The mass-weighted mean diameter ($D_m$) distribution curve in summer is distinctly different from winter season (Figure 4c). The $D_m$ distribution shows peak PDF values around 1.0–1.4 mm in summer season and around 0.7–0.9 mm in winter season (Figure 4c). The probability distribution
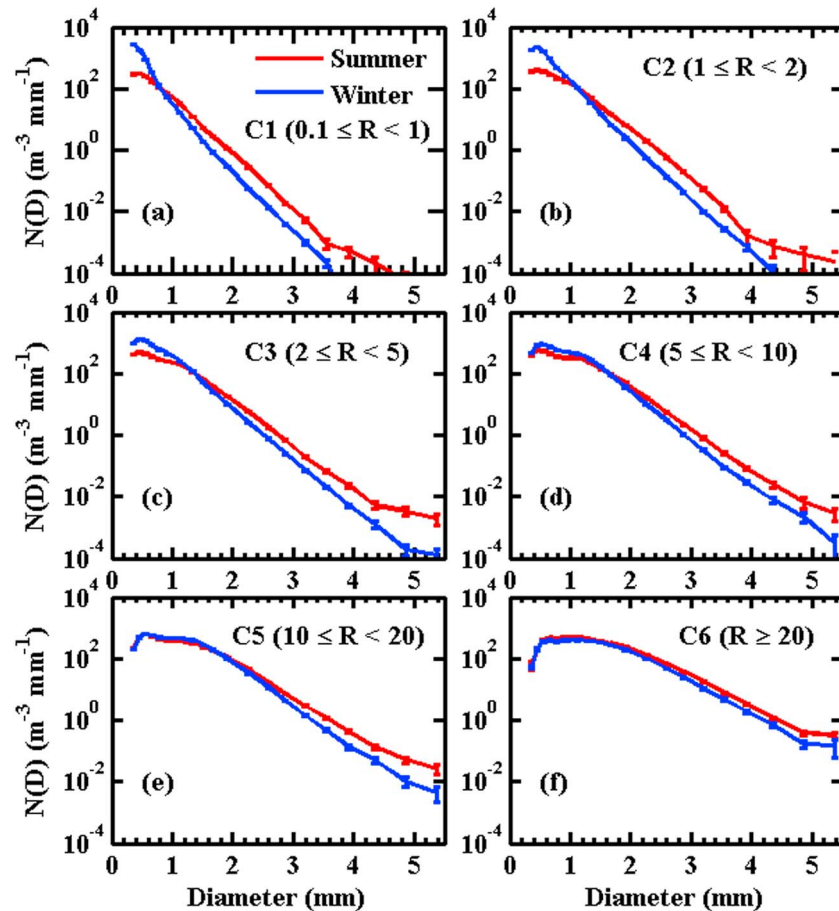


**Figure 5.** Average raindrop spectra for winter (blue) and summer (red) rainfall in (a–f) six rain rate (*R*) classes (C1:0.1-1, C2:1:2, C3:2:5, C4:5-10, C5:10-20, and C6: >20 mm/hr).
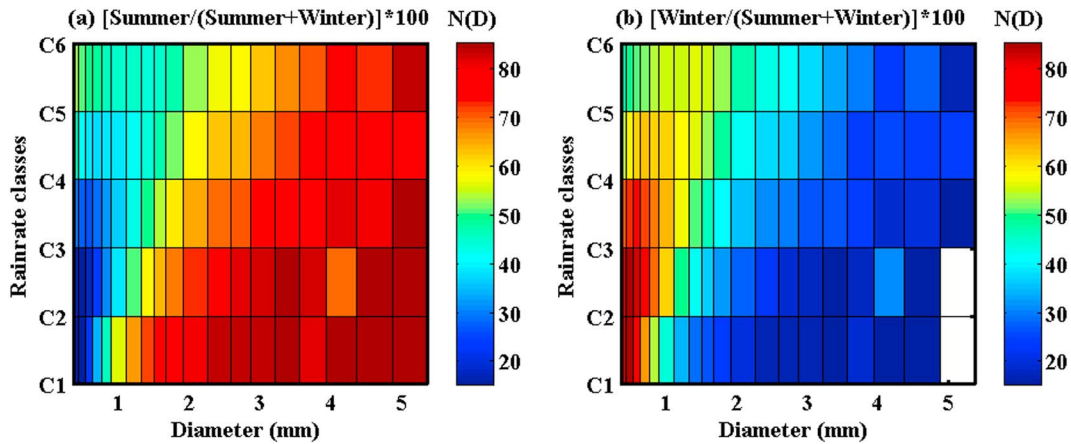
**Figure 6.** Percentage parameter, $\delta(D, R)$ for (a) summer and (b) winter rainfall.

of normalized intercept parameter ($\log_{10}N_w$) shows a higher percentage at lower $\log_{10}N_w$ values in summer and a higher percentage at higher $\log_{10}N_w$ values in winter (Figure 4d). The peak value of shape parameter ($\mu$) distribution curve appears at 5 for summer and at 5.2 for the winter season. The distribution of $\mu$ is higher in winter than summer season for $\mu > 5.7$ (Figure 4e). The slope parameter ($\Lambda$) distribution curve shows a similar pattern to that of the shape parameter with higher distribution in winter than summer for $\Lambda > 7$ mm$^{-1}$ (Figure 4f). Larger $\mu$ and $\Lambda$ in winter than summer indicates a narrower RSD shape, and this characteristic can be seen in Figure 3. Overall, there are distinct differences between probability distributions of summer and winter rain parameters. The distribution of rain rate, mass-weighted mean diameter, and the shape parameter highlights the dominance of light, small-drop rainfall with narrow size spectra in the winter than the summer season. To further confirm the differences between summer and winter rain parameters, statistical Student's $t$ test is performed for the above six rain parameters ($\log_{10}R$, $\log_{10}W$, $D_m$, $\log_{10}N_w$, $\mu$, and $\Lambda$) and the results are provided in Table 3. The test results disprove the null hypothesis $H_0$($\log_{10}R_{summer}$ = $\log_{10}R_{winter}$; $\log_{10}W_{summer}$ = $\log_{10}W_{winter}$; $D_{m\_summer}$ = $D_{m\_winter}$; $\log_{10}N_{w\_summer} = \log_{10}N_{w\_winter}$; $\mu_{summer} = \mu_{winter}$; $\Lambda_{summer} = \Lambda_{winter}$) and confirm the alternative hypothesis $H_1$ ($\log_{10}R_{summer}$ ≠ $\log_{10}R_{winter}$; $\log_{10}W_{summer}$ ≠ $\log_{10}W_{winter}$; $D_{m\_summer}$ ≠ $D_{m\_winter}$; $\log_{10}N_{w\_summer} \neq \log_{10}N_{w\_winter}$; $\mu_{summer} \neq \mu_{winter}$; $\Lambda_{summer} \neq \Lambda_{winter}$) with confidence levels of 0.05 and 0.01.

### 3.2. RSD in Different Rain Rate Classes

To further investigate the RSD differences between summer and winter, rainfall in both seasons are divided into six rain rate class (C1: $0.1 \leq R < 1$, C2: $1 \leq R < 2$, C3: $2 \leq R < 5$, C4: $5 \leq R < 10$, C5: $10 \leq R < 20$, and C6: $\geq 20$ mm/hr) by following Tokay and Short (1996) rain rate classification criteria. Rain rate statistics for each class in summer and winter rainfall are provided in Table 4. For each rain rate class, variations in raindrop concentration ($N(D)$, m$^{-3}$ mm$^{-1}$) with raindrop size (D, mm) for summer and winter are depicted in Figure 5. In the first rain rate class (Figure 5a, C1: $0.1 \leq R < 1$ mm/hr), small-size drops (D < 1 mm) have higher a concentration in winter and lower concentration in summer and a reverse pattern can be seen for the midsize and large drops (D > 1 mm). Raindrops of diameter smaller than 1.2 mm have a lower concentration, and raindrops larger than 1.2 mm have a higher concentration in summer as compared to winter rainfall in the second rain rate class (Figure 5b, C2: $1 \leq R < 2$ mm/hr). In third rain rate class (Figure 5c, C3: $2 \leq R < 5$ mm/hr), raindrops of diameter less than 1.4 mm are more in winter than summer rainfall, and raindrops above 1.4 mm diameter are more in summer than winter rainfall. Raindrops above 1.6 mm diameter have a higher concentration in summer than winter in the fourth rain rate class (Figure 5d,
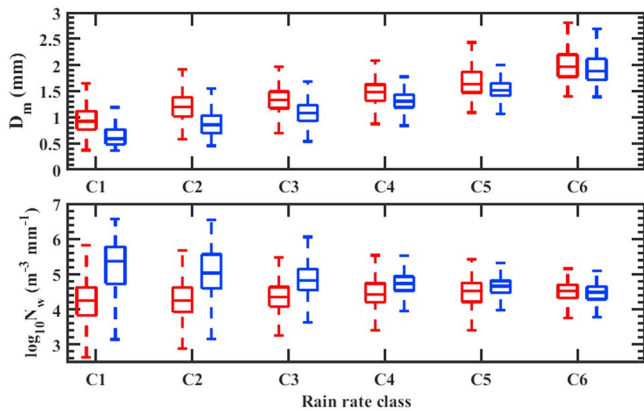


**Figure 7.** Variation of mass-weighted mean diameter, $D_m$ (mm) and normalized intercept parameter, $\log_{10}N_w$ (m$^{-3}$ mm$^{-1}$) in six rain rate classes (C1:0.1-1, C2:1:2, C3:2:5, C4:5-10, C5:10-20, and C6: >20 mm/hr) of summer (red) and winter (blue) rainfall. The center line of the box indicates the median, and the bottom and top lines of the box indicate the 25th and 75th percentiles, respectively. The bottom and top of the dashed vertical lines indicate the 5th and 95th percentiles, respectively.

**Table 5**
*Mean and Standard Deviation (Std) Values of $D_m$, $\log_{10}N_w$, $\mu$, and $\Lambda$ for Summer and Winter Rainfall in Different Rain Rate Classes*

| Rain rate class | Summer | | | | | | | | Winter | | | | | | | |
|---|---|---|---|---|---|---|---|---|---|---|---|---|---|---|---|---|
| | $D_m$ (mm) | | $\log_{10}N_w$ (m$^{-3}$ mm$^{-1}$) | | $\mu$ (−) | | $\Lambda$ (mm$^{-1}$) | | $D_m$ (mm) | | $\log_{10}N_w$ (m$^{-3}$ mm$^{-1}$) | | $\mu$ (−) | | $\Lambda$ (mm$^{-1}$) | |
| | Mean | Std | Mean | Std | Mean | Std | Mean | Std | Mean | Std | Mean | Std | Mean | Std | Mean | Std |
| C1 | 0.97 | 0.28 | 4.23 | 0.62 | 8.25 | 10.5 | 14.37 | 14.44 | 0.65 | 0.23 | 5.2 | 0.72 | 15.63 | 14.82 | 36.91 | 35.88 |
| C2 | 1.22 | 0.29 | 4.27 | 0.53 | 5.13 | 5.86 | 7.91 | 5.15 | 0.88 | 0.25 | 5.06 | 0.64 | 6.37 | 6.54 | 13.26 | 10.08 |
| C3 | 1.35 | 0.31 | 4.36 | 0.48 | 4.87 | 4.95 | 6.86 | 3.89 | 1.09 | 0.24 | 4.86 | 0.49 | 4.79 | 5.16 | 8.56 | 5.42 |
| C4 | 1.51 | 0.3 | 4.44 | 0.42 | 5.37 | 4.57 | 6.47 | 3.34 | 1.32 | 0.22 | 4.73 | 0.35 | 5.37 | 4.89 | 7.27 | 3.76 |
| C5 | 1.72 | 0.37 | 4.45 | 0.43 | 4.89 | 3.57 | 5.42 | 2.61 | 1.56 | 0.26 | 4.62 | 0.32 | 6.15 | 4.33 | 6.69 | 3.09 |
| C6 | 2.05 | 0.43 | 4.45 | 0.37 | 4.25 | 2.75 | 4.17 | 1.48 | 1.98 | 0.43 | 4.42 | 0.38 | 5.26 | 4.08 | 4.82 | 1.99 |
| All classes | 1.18 | 0.42 | 4.29 | 0.57 | 6.75 | 8.59 | 10.89 | 11.65 | 0.78 | 0.31 | 5.11 | 0.69 | 12.29 | 13.4 | 28.1 | 32.13 |

C4: $5 \leq R < 10$ mm/hr). In the remaining two rain rate classes (Figure 5e, C5: $10 \leq R < 20$ mm/hr; Figure 5f, C6: $R \geq 10$ mm/hr), summer rainfall has a higher concentration than winter for the raindrops above 2-mm diameter. For both seasons, with the increase in rain rate class, the breadth of RSD shape increases, the tail of RSD shifts toward the larger diameter, and the concentration of small drops decreases (Figure 5). Nevertheless, in all rain rate classes, the summer rainfall has a higher concentration of midsize and large drops than winter rainfall.

Moreover, a percentage parameter $\delta(D, R)$ is considered to emphasize the clear differences in RSD characteristics of summer and winter rainfall. The $\delta(D, R)$ is the ratio of the mean raindrop concentration in one season ($N(D)$ of summer/winter) at a diameter $D$ and a rain rate $R$ to the sum of the mean raindrop concentrations in both seasons ($N(D)$ of summer and winter). The percentage parameter chosen in the present study is similar to that of Seela et al. (2017); however, different rain rate classes are considered in this study. Variations in $\delta(D, R)$ of summer and winter rainfall are depicted in Figure 6. From the figure, we can notice distinct variations between raindrop concentrations of summer and winter rainfall. The contribution of small drops (<1-mm diameter) is predominant in winter than summer, whereas the contribution of midsize and large drops (>1 mm) is higher in summer rainfall as compared to winter rainfall.

Variation of mass-weighted mean diameter ($D_m$) and normalized intercept parameter ($\log_{10}N_w$) in six rain rate classes of summer and winter rainfall is provided in Figure 7 with box-whisker plot. The center line of the box indicates the median, and the bottom and top lines of the box indicate the 25th and 75th percentiles, respectively. The bottom and top of the dashed vertical lines indicate the 5th and 95th percentiles, respectively. In both summer and winter rainfall, $D_m$ values are increasing with the increase in rain rate class. This could be due to the decrease in small drop concentration and an increase in midsize and large drop concentration with the increase of rain rate class. Apart from this, in all the rain rate classes, summer rainfall has higher $D_m$ values than the winter season. On the other hand, except in the last rain rate class, winter
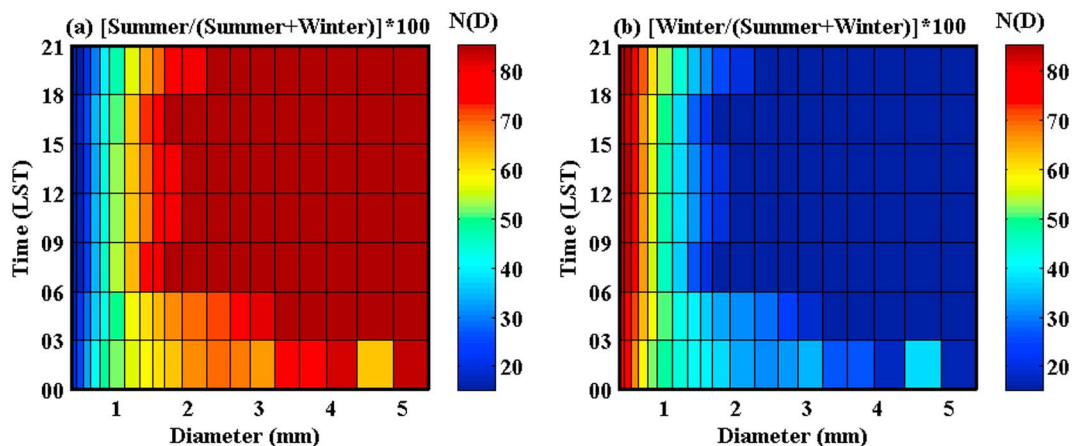


**Figure 8.** Percentage parameter, $\delta(D, T)$ for (a) summer and (b) winter rainfall. LST= local standard time.
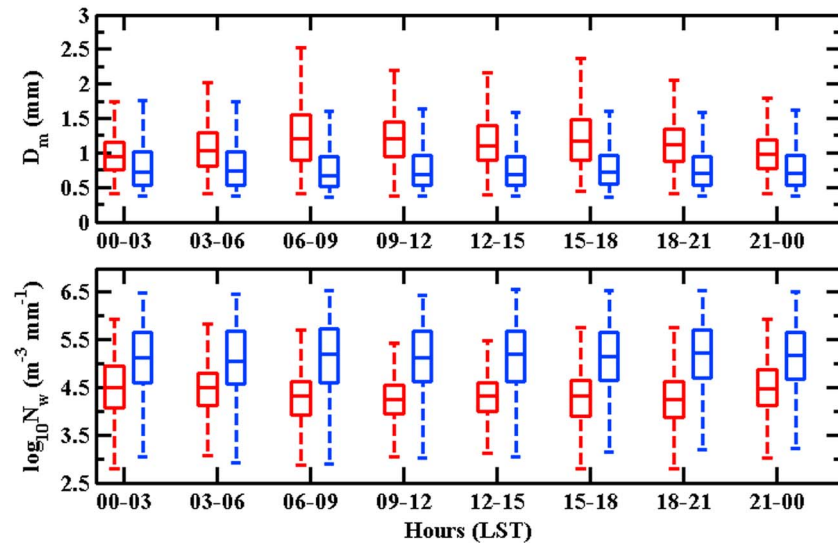
**Figure 9.** The 3-hourly variation of mass-weighted mean diameter, $D_m$ (mm) and normalized intercept parameter, $\log_{10}N_w$ ($m^{-3}$ $mm^{-1}$) in summer (red) and winter (blue) rainfall. The 3-hourly observations represented in above plot are in local time (UTC + 8 hr). LST = local standard time.

rainfall has higher $\log_{10}N_w$ values than summer rainfall in all rain rate class. Mean and standard deviation values of $D_m$, $\log_{10}N_w$, $\mu$, and $\Lambda$ in six rain rate classes are provided in Table 5. From the table, it can be clearly seen that the summer rainfall has a higher mean $D_m$ and a lower $\log_{10}N_w$, $\mu$, and $\Lambda$ than winter. In both summer winter seasons, mean values of shape parameter ($\mu$) show an irregular decreasing trend with the increase in rain rate class. On the other hand, the mean slope parameter decreases with the increase in rain rate class.

### 3.3. Diurnal Variation of RSD

To examine the diurnal differences between summer and winter RSD, a percentage parameter $\delta(D, T)$ is considered for the 3-hourly (00–03, 03–06, 06–09, 09–12, 12–15, 15–18,15–21, and 21–00 hr, in local time) RSD distribution. The $\delta(D, T)$ is the ratio of mean raindrop concentration in one season ($N(D)$ of summer/winter) at a diameter $D$ and a three-hours' time to the sum of mean raindrop concentrations in both seasons ($N(D)$ of summer and winter). The variations of number concentration with drop diameter in 3-hourly time interval for summer and winter rainfall are shown with the percentage parameter, $\delta(D, T)$ in Figure 8. From the figure, for every 3-hr interval, we can clearly notice that the summer season is predominant with the midsize and large drops (Figure 8a) and the winter season with small drops (Figure 8b). The 3-hourly variations of mass-weighted mean diameter ($D_m$) and normalized intercept parameter ($\log_{10}N_w$) in summer and winter seasons are depicted in Figure 9 with box-whisker plot. The 3-hourly variations show higher $D_m$ and lower $\log_{10}N_w$ values in summer than the winter season, as well. For both the seasons, there are no much diurnal variations of $D_m$ or $\log_{10}N_w$ for a given season; nonetheless, we can notice distinct differences in $D_m$ or $\log_{10}N_w$ values between summer and winter.



**Figure 10.** Mean raindrop concentration in stratiform and convective regimes of summer and winter rainfall.

### 3.4. Stratiform and Convective RSD

RSD characteristics of a precipitation significantly vary from stratiform to convective regime. Numerous researchers found clear distinctions between stratiform and convective regimes. For example, sequential variations in raindrop parameters from convective to stratiform were reported by Tokay and Short (1996). Adopting different Z-R relationships
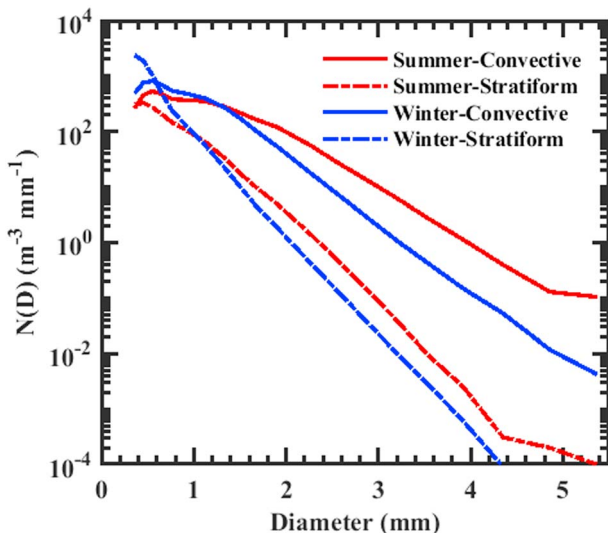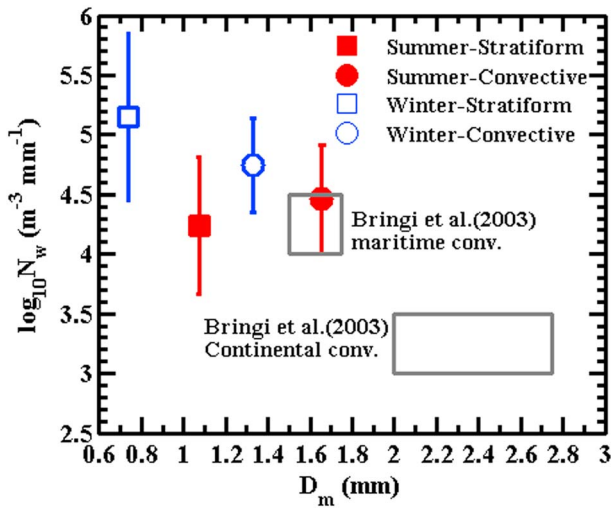
**Figure 11.** Variation of normalized intercept parameter, $\log_{10}N_w$ ($m^{-3}$ $mm^{-1}$) with mass-weighted mean diameter, $D_m$ (mm) in stratiform and convective regimes of summer and winter rainfall.

for stratiform and convective regimes has been a common practice for decades before Ulbrich and Atlas (2007). The reason is that RSD are expected to be different for stratiform and convective regimes. See, for example, Waldvogel (1974), Tokay and Short (1996), and Maki et al. (2001). RSD characteristics of different rain types over a wide range of climatic regimes were studied by Bringi et al. (2003), and they found distinct variations between stratiform and convective regimes of the maritime and continental clusters. As the microphysical characteristics of raindrop spectra vary from stratiform to convective precipitation, we analyzed the RSD of summer and winter rainfall by classifying into stratiform and convective regimes. There are many rain classification schemes proposed by previous researchers using different ground-based instruments like disdrometer, profiler, and radar (Bringi et al., 2003; Campos et al., 2006; Das et al., 2017; Krishna et al., 2016; Steiner et al., 1995; Thurai et al., 2016; Tokay & Short, 1996). In the present study, summer and winter rainfall are classified into stratiform and convective type by adopting the Bringi et al. (2003) classification criteria. They classified the precipitation into convective if the mean rain rate ($R_{mean}$) of five consecutive 2-min RSD samples is >0.5 mm/hr and standard deviation of rain rate ($\sigma_R$) <1.5 mm/hr and the rest as stratiform. In the current work, summer and winter rainfall are separated into stratiform and convective type by using 10 consecutive 1-min RSD samples.

Variations in RSD of convective and stratiform regimes of summer and winter rainfall are illustrated in Figure 10. For both summer and winter rainfall, drop concentration of convective regime is higher than the stratiform regime for the raindrops with diameter greater than 1 mm. In both summer and winter rainfall, convective regimes have relatively broad distributions with concave downward shape than the stratiform type, which is partly due to the collisional breakup of the large drops in convective type (Hu & Srivastava, 1995). Stratiform regimes have nearly exponential distribution with less tendency toward downward concavity. Present distributions in stratiform and convective regimes are in accordance with the observations of previous researchers (B. Chen et al., 2013; Jayalakshmi & Reddy, 2014; Krishna et al., 2016; Niu et al., 2010). For both stratiform and convective type of precipitation, a higher concentration of small drops and a lower concentration of midsize and large drops is observed in winter than summer rainfall.

Variations in $D_m$ and $\log_{10}N_w$ values of stratiform and convective regimes of summer and winter rainfall are provided in Figure 11. The convective precipitations are associated with higher $D_m$ as compared to stratiform precipitation for both summer and winter seasons. Besides that, summer rainfall has a higher $D_m$ and a lower $\log_{10}N_w$ values than winter rainfall for both the precipitation types (stratiform and convective). Mean and standard deviation values of $D_m$, $\log_{10}N_w$, $\mu$, and $\Lambda$ in stratiform and convective regimes of both the seasons are given in Table 6. Bringi et al. (2003) measured $\log_{10}N_w$ and $D_m$ values for a wide range of locations. For convective rain, they found $D_m$ ($\log_{10}N_w$) ranging from 1.5 to 1.75 mm (4 to 4.5 $m^{-3}$ $mm^{-1}$) for the maritime-like cluster and 2 to 2.75 mm (3 to 3.5 $m^{-3}$ $mm^{-1}$) for the continental-like cluster. These maritime and continental convective clusters are shown with gray-colored rectangular boxes in Figure 11. Comparison of present results with Bringi et al. (2003) convective clusters (maritime-like and continental-like) shows that the mean $D_m$ and $\log_{10}N_w$ values of summer convective rainfall are somewhat similar to the maritime-like

**Table 6**
*Mean and Standard Deviation (Std) Values of $D_m$, $\log_{10}N_w$, $\mu$, and $\Lambda$ for Stratiform and Convective Precipitations of Summer and Winter*

| | Summer | | | | | | | | Winter | | | | | | | |
|---|---|---|---|---|---|---|---|---|---|---|---|---|---|---|---|---|
| | $D_m$ (mm) | | $\log_{10}N_w$ ($m^{-3}$ $mm^{-1}$) | | $\mu$ (−) | | $\Lambda$ ($mm^{-1}$) | | $D_m$ (mm) | | $\log_{10}N_w$ ($m^{-3}$ $mm^{-1}$) | | $\mu(-)$ | | $\Lambda$ ($mm^{-1}$) | |
| Rain type | Mean | Std | Mean | Std | Mean | Std | Mean | Std | Mean | Std | Mean | Std | Mean | Std | Mean | Std |
| Stratiform | 1.07 | 0.32 | 4.24 | 0.57 | 4.38 | 3.27 | 6.11 | 2.93 | 0.74 | 0.28 | 5.15 | 0.69 | 4.06 | 4.01 | 6.63 | 3.50 |
| Convective | 1.65 | 0.49 | 4.46 | 0.46 | 4.74 | 3.51 | 5.24 | 2.57 | 1.33 | 0.34 | 4.75 | 0.39 | 5.56 | 4.19 | 6.86 | 3.26 |

**Table 7**

*Radar Reflectivity-Rain Rate (Z = A\*R$^b$) Relations for Summer and Winter Seasons Rainfall of North Taiwan*

| Precipitation type | Summer | Winter |
|---|---|---|
| Stratiform | $Z = 276.13\,R^{1.41}$ | $Z = 127.67\,R^{1.54}$ |
| Convective | $Z = 237.88\,R^{1.41}$ | $Z = 142.94\,R^{1.52}$ |
| Total | $Z = 266.42\,R^{1.38}$ | $Z = 129.76\,R^{1.55}$ |

clusters. However, the winter convective rainfall has lower $D_m$ and higher $\log_{10}N_w$ than the convective clusters of Bringi et al. (2003).

### 3.5. Radar Reflectivity and Rain Rate (*Z-R*) Relations

The coefficient (*A*) and exponent (*b*) of radar reflectivity-rain rate ($Z = A\*R^b$) relations were found to vary with geographical location, atmospheric condition, and type of instrument (Campos & Zawadzki, 2000; Rosenfeld & Ulbrich, 2003) and strongly depend on RSD variability. The uncertainties in estimating rain rate from weather radars can be minimized with well-established radar reflectivity and rain rate (*Z-R*) relations for a given location, season, and type of precipitation. Therefore, it is necessary to investigate the *Z-R* relations in summer and winter rainfall for the better understanding of their variability and to further improve the radar QPE. The *Z-R* relations can provide microphysical process involved with raindrops. In $Z = A\*R^b$ relation, the coefficient *A* deduces the presence of drops with big or small size and the exponent *b* represents the microphysical process. If *b* is greater than unity, then collision-coalescence (size or mixed controlled) is the characteristics feature. If *b* is equal to unity, collision, coalescence, and breakup process (number controlled) are associated with homogeneous rainfall (Atlas et al., 1999; Atlas & Williams, 2003; Steiner et al., 2004). The radar reflectivity and rain rate (*Z-R*) relations of summer and winter rainfall are obtained by applying linear regression to logarithmic values of rain rate (*R*, mm/hr) and radar reflectivity (*Z*, mm$^6$/m$^3$) and are provided in Table 7. A clear difference in coefficient and exponent values of *Z-R* relations can be noticed between summer and winter rainfall. The *Z-R* relations obtained in this study are found to be different from that of the relations currently using in high-resolution QPE system for Taiwan (J. Zhang et al., 2009). This strongly suggests that there is need to adopt modified *Z-R* relations in computation of Taiwan rainfall by QPE.

### 3.6. Mu-Lambda (*μ-Λ*) Relations

The mean behavior of RSD parameters and actual RSD characteristics can be understood with the help of *μ-Λ* relations, and these relations are useful in retrieving and reducing the bias in rain parameters from remote measurements (G. Zhang et al., 2003). The *μ-Λ* relations were found to vary from location to location (Chu & Su, 2008; W.-Y. Chang, Wang, & Lin, 2009; Kumar et al., 2011; B. Chen et al., 2013; B. Chen, Wang, & Gong, 2016) and depend on the rain microphysics (Atlas & Ulbrich, 2006). An empirical polynomial *μ-Λ* relation ($\Lambda = 0.0365\,\mu^2 + 0.735\,\mu + 1.935$) was proposed by Brandes et al. (2003) and G. Zhang et al. (2003) for the precipitation with rain rate greater than 5 mm/hr. In the present study, the *μ-Λ* relations are obtained by applying threshold criteria (drops counts > 1,000 and rain rate > 5 mm/hr) proposed by Brandes et al. (2003) and
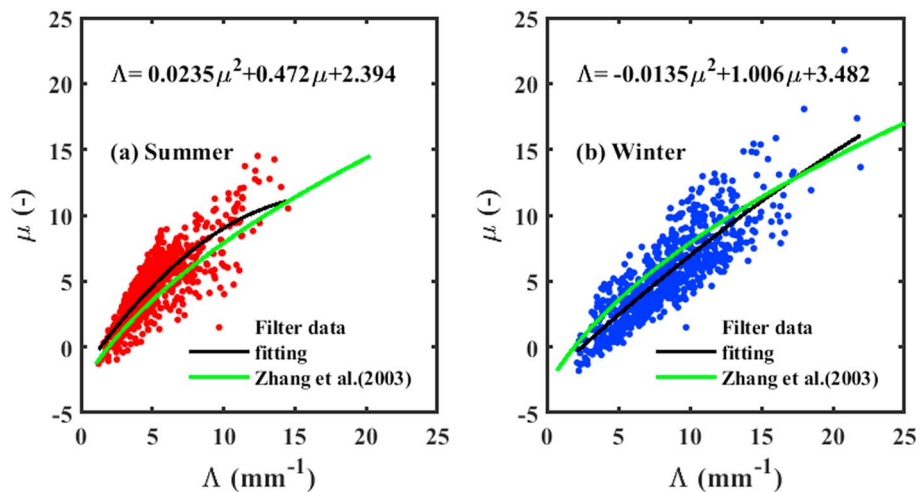


**Figure 12.** Scatterplots of *μ* versus Λ for (a) summer and (b) winter rainfall of north Taiwan. The red and blue solid circles in summer and winter, respectively, are data points with rain rate > 5 mm/hr. The black line and the equation shown on figures represent a least squares fit to the filtered data. The green line corresponds to the *μ-Λ* relation of G. Zhang et al. (2003).

**Table 8**
*The $\mu$-$\Lambda$ Relations of Current Study and Other Parts of the World*

| Reference | Location | Precipitation type/precipitation period/season | Disdrometer type | $\mu$-$\Lambda$ relations |
|---|---|---|---|---|
| Present study | NCU, north Taiwan | Summer | Joss-Waldvogel disdrometer | $\mu = -0.0444\,\Lambda^2 + 1.549\,\Lambda - 2.054 \Lambda = 0.0235\,\mu^2 + 0.472\,\mu + 2.394$ |
| Present study | NCU, north Taiwan | Winter | Joss-Waldvogel disdrometer | $\mu = -0.0079\,\Lambda^2 + 1.019\,\Lambda - 2.467 \Lambda = -0.0135\,\mu^2 + 1.006\,\mu + 3.482$ |
| G. Wen, Xiao, et al. (2017) | Beijing, China | Summer (June–September) | Two-dimensional Video disdrometer | $\Lambda = 0.019\,\mu^2 + 0.795\,\mu + 2.033$ |
| J. Wen, Zhao, et al. (2017) | Jiangning, Eastern China | Squall lines | Two-dimensional Video disdrometer | $\mu = -0.0203\,\Lambda^2 + 1.6023\,\Lambda - 2.5455$ |
| Chen et al. (2017) | Tibetan Plateau | Summer (June–August) | Parsivel disdrometer | $\Lambda = 0.0217\,\mu^2 + 1.090\,\mu + 1.706 \mu = -0.0044\,\Lambda^2 + 0.7646\,\Lambda - 0.4898$ |
| B. Chen, Wang, and Gong (2016) | Shandong Province, Eastern China | Squall line | Thies disdrometer | $\Lambda = 0.0585\,\mu^2 + 0.812\,\mu + 1.934$ |
| Lam et al. (2015) | Malaysia | Convective events (1992–1994) | Joss-Waldvogel disdrometer | $\Lambda = 0.04102\,\mu^2 + 0.3103\,\mu + 1.74$ |
| Tang et al. (2014) | Beijing, North China | July–October | Parsivel disdrometer | $\Lambda = 0.0075\,\mu^2 + 0.723\,\mu + 1.1721$ |
|  | Zhangbei, North China | April–August | Parsivel disdrometer | $\Lambda = 0.0097\,\mu^2 + 0.7226\,\mu + 1.7415$ |
|  | Yangjiang, South China | July to August | Parsivel disdrometer | $\Lambda = 0.0240\,\mu^2 + 0.4596\,\mu + 1.9920$ |
| Chen et al. (2013) | Nanjing, Eastern China | Meiyu (June–July) | Parsivel disdrometer | $\Lambda = 0.0149\,\mu^2 + 0.491\,\mu + 2.015$ |
| Chen et al. (2012) | Fujian | Typhoon Morakot | Parsivel disdrometer | $\Lambda = 0.0253\,\mu^2 + 0.633\,\mu + 1.524$ |
| Kumar et al. (2011) | Singapore | 14 rain events (August 1994 to September 1995, excluding June and July 1995) | Joss-Waldvogel disdrometer | $\Lambda = 0.036\,\mu^2 + 0.432\,\mu + 1.507$ |
| W.-Y. Chang, Wang, and Lin (2009) | NCU, north Taiwan | Typhoons | Two-dimensional Video disdrometer | $\Lambda = 0.0136\,\mu^2 + 0.6984\,\mu + 1.5131$ |
| Chu and Su (2008) | NCU, north Taiwan | four types of weather systems (typhoon, cold front, stationary front, and convective cloud) | Two-dimensional Video disdrometer | $\Lambda = 0.017\,\mu^2 + 1.303\,\mu + 1.833$ (for low order moment) $\Lambda = 0.007\,\mu^2 + 1.362\,\mu + 1.569$ (for low order moment) |
| G. Zhang et al. (2003) Brandes et al. (2003) | Florida | Summer of 1998 | 2-D video disdrometer | $\Lambda = 0.0365\,\mu^2 + 0.735\,\mu + 1.935$ |

*Note.* NCU = National Central University.

G. Zhang et al. (2003). This method removes unrealistic data points (with negative and very large values of $\Lambda$) caused due to quantifying errors or limitation of the filtering approach. The scatterplot between slope ($\Lambda$) and shape parameter ($\mu$) values of summer and winter precipitation is plotted in Figures 12a and 12b, respectively. The $\mu$-$\Lambda$ relations derived in the present study and other parts of the globe are provided in Table 8. From the table, we can notice that the $\mu$-$\Lambda$ relations of summer are unlike to winter and are different from the other observational studies. The present study confirms the opinion of the previous researchers; that is, the $\mu$-$\Lambda$ relations varies in different precipitation types and climatic regimes.

## 4. Discussion

Summer and winter seasons of Taiwan are influenced by two major low-level wind patterns. Summer is associated with southwesterly monsoon flow, whereas winter is associated with northeasterly monsoon flow (C. S. Chen & Chen, 2003; T.-C. Chen et al., 1999). Southwesterly monsoon flow in summer brings warm, moist maritime air resulting potentially unstable atmosphere over Taiwan (C. S. Chen & Chen, 2003). Summer rainfall is mostly associated with tropical storms, mesoscale disturbances, and afternoon convective showers due to diurnal heating cycle over western windward slopes of the central mountain range (Yang, 2000). Northeasterly monsoon flow brings a number of cold fronts with sharp temperature drops over Taiwan in the winter season (Yen & Chen, 2002). Low moisture content and relatively stable atmospheric
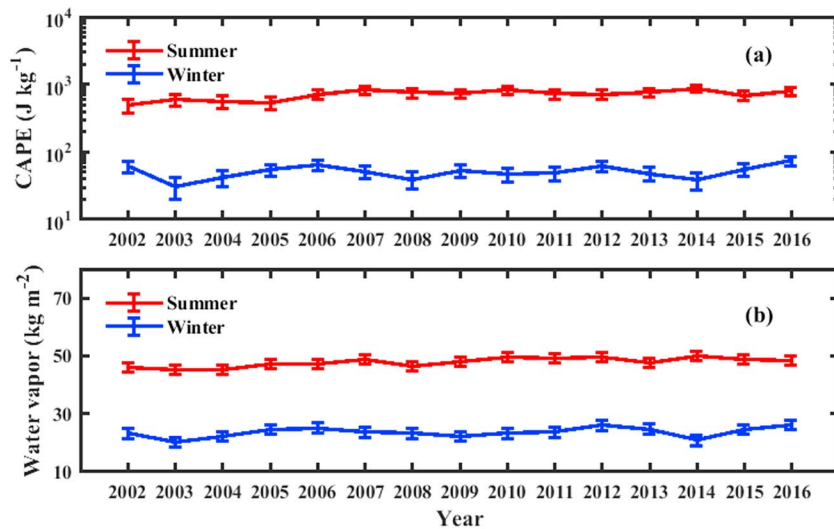
**Figure 13.** Annual variations of (a) convective available potential energy, CAPE (J/kg) and (b) vertical integral water vapor (kg/m$^2$) obtained from ERA-Interim for summer and winter seasons.

stratifications can be seen in the winter season. CAPE and vertical integral of water vapor for summer (16 June to 31 August) and winter (December–February) seasons over north Taiwan (24°–25.2°N and 121°–121.9°E) from 2002 to 2016 are obtained from ERA-Interim and are depicted in Figure 13. From the figure, it can be clearly seen that the summer has higher CAPE and water vapor values than winter, confirming that the precipitating clouds in summer are more convective with severe updrafts and downdrafts. Latent heat released during the phase change of hydrometeors drives the updrafts, whereas the cooling induced by melting and evaporation initiates the downdraft. The convective clouds in summer are extended to deeper altitudes than winter and are confirmed by the higher storm heights (STHs) and BBHs, obtained from the TRMM satellite (Figure 14). These storm and bright bands heights are also obtained over the JWD observational site (24°–25.2°N and 121°–121.9°E). Strong convective activity in summer clouds shoots the water vapor to higher altitude resulting in faster growth of ice crystals above the melting layer. In deep convective clouds of summer (Figure 14), ice crystals grow to large snowflakes through vapor deposition and aggregation, which in turn produces relatively large drops while crossing the melting level. These bigger ice crystals melt to
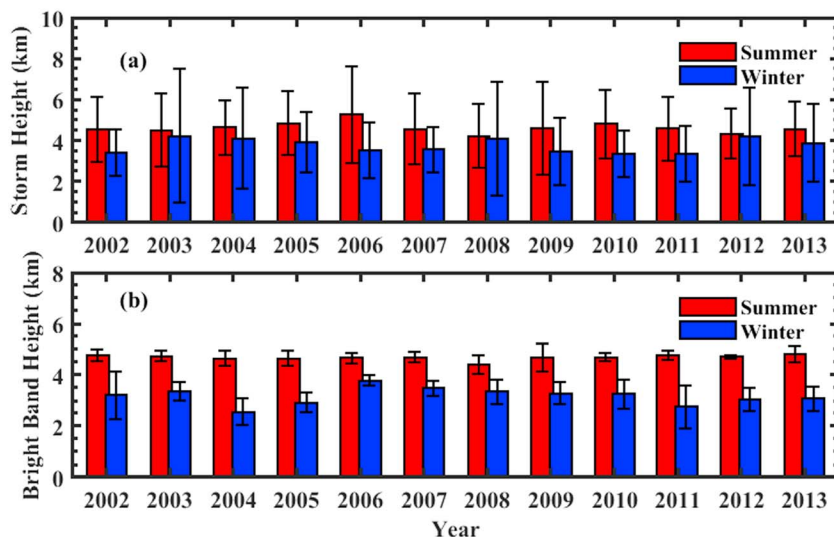


**Figure 14.** Annual variation of (a) mean storm top height and (b) bright band height during summer and winter seasons obtained from Tropical Rainfall Measuring Mission precipitation radar 2A23 product.
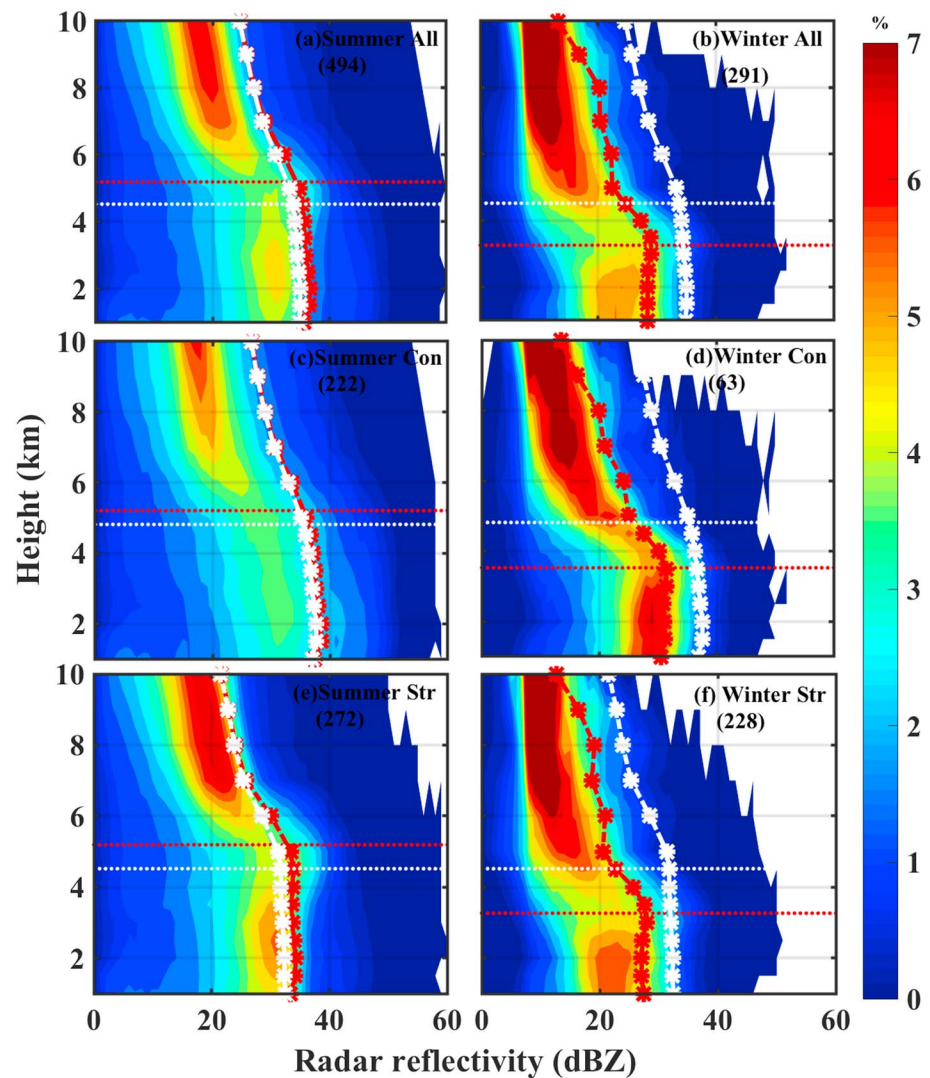
**Figure 15.** Contoured frequency-by-altitude diagram of radar reflectivity from six ground-based radars for (a) summer, (b) winter, (c) summer convective, (d) winter convective, (e) summer stratiform, and (f) winter stratiform rainfall. Mean freezing level heights of summer and winter seasons (2005–2014) are calculated from nearest radiosonde stations (Banqiao, 121.441°E, 24.997°N station no. 46692; Hualien, 121.619°E, 23.989°N, station no. 46699) data. The horizontal white dotted line in Figures 15a–15f is the average of the melting layer heights of summer and winter seasons. The horizontal red dotted line in Figures 15a, 15c, and 15e is the mean melting layer of summer season, and the horizontal red dotted line in Figures 15b, 15d, and 15f is the mean melting layer of winter season. The vertical white star dotted line (in Figures 15a and 15b) is the average of the radar reflectivity profiles of summer and winter rainfall. The vertical red star dotted line in Figure 15a is the mean vertical profile of summer rainfall, and vertical red star dotted line in Figure 15b is the mean vertical profile of winter rainfall. The vertical white star dotted line (in Figured 15c and 15d) is the average of the radar reflectivity profiles of convective regimes of summer and winter rainfall. The vertical red star dotted line in Figure 15c is the mean vertical profile of summer convective rainfall, and vertical red star dotted line in Figure 15d is the mean vertical profile of winter convective rainfall. Similarly, the vertical white star dotted line (in Figures 15e and 15f) is the average of the radar reflectivity profiles of stratiform regimes of summer and winter rainfall. The vertical red star dotted line in figure 15e is the mean vertical profile of summer stratiform rainfall, and vertical red star dotted line in Figure 15f is the mean vertical profile of winter stratiform rainfall.

precipitate as bigger raindrops at the ground (Heymsfield et al., 2002; Rosenfeld & Ulbrich, 2003). In addition to riming process above the melting layer, drop sorting and enhanced collision-coalescence process occur below the melting layer of deep convective clouds of summer. Smaller drops are lifted up into divergent regions through strong updrafts and allow bigger drops to fall. An increase in the collision-coalescence process is aided by updraft by holding the small drops aloft result in large $D_m$ values at the ground.
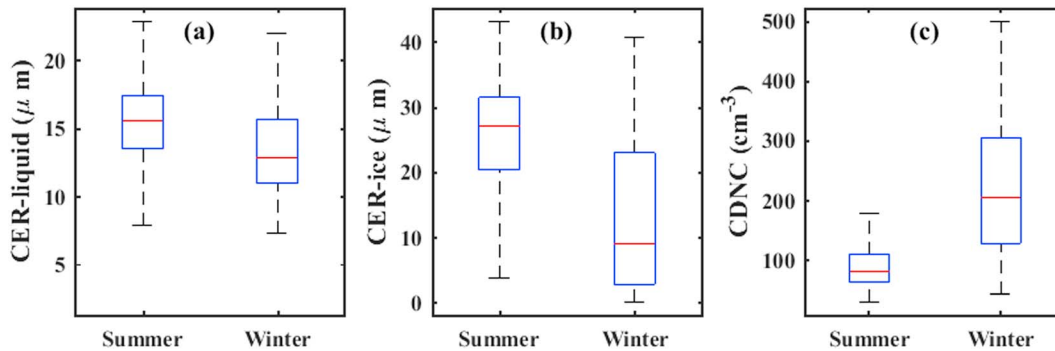
**Figure 16.** Box and whisker plots of cloud effective radii (CER, μm) values of (a) liquid, (b) ice particles, and (c) cloud droplet number concentration (CDNC, cm$^{-3}$) for summer and winter seasons. The centerline of the box indicates the median, and the bottom and top lines of the box indicate the 25th and 75th percentiles, respectively. The bottom and top of the dashed vertical lines indicate the 5th and 95th percentiles, respectively.

To confirm the above-mentioned reasons and to look into more detail about the cloud and rain processes in summer and winter rainfall, radar reflectivity profiles available from 2005 to 2014 for the disdrometer measurement period are used. The contoured frequency-by-altitude diagram (CFAD; Yuter & Houze, 1995) of radar reflectivity of summer (285 profiles) and winter (2475 profiles) seasons and their precipitation type (Tokay et al., 1999) is shown in Figure 15. Melting layer height of summer and winter seasons is obtained from nearest radiosonde stations data (Banqiao, 121.441°E, 24.997°N station no. 46692; Hualien, 121.619°E, 23.989°N, station no. 46699). The average of the melting layer heights of summer and winter seasons is shown with a horizontal white dotted line in summer (Figures 15a, 15c, and 15e) and winter (Figures 15b, 15d, and 15f) CFADs. This white dotted line is used as a reference to compare the melting layer heights of summer and winter seasons. The horizontal red dotted line in Figures 15a, 15c, and 15e is the mean melting layer of the summer season, and the horizontal red dotted line in Figures 15b, 15d, and 15f is the mean melting layer of the winter season. From the figure, it is observed that the mean melting layer height in summer is higher as compared to winter. Because of sufficiently higher 0 °C isotherm level in summer, RSD in summer evolves into an equilibrium distribution under the influence of collision, coalescence, and breakup processes (Atlas & Ulbrich, 2006; Hu & Srivastava, 1995). The average of reflectivity profiles of summer and winter rainfall is depicted with white star dotted line in Figures 15a and 15b. Similarly, the white star dotted line in Figures 15c and 15d (Figures 15e and 15f) denotes the average of reflectivity profiles of both the seasons' convective (stratiform) rainfall. The mean reflectivity profile of summer rainfall and winter rainfall is
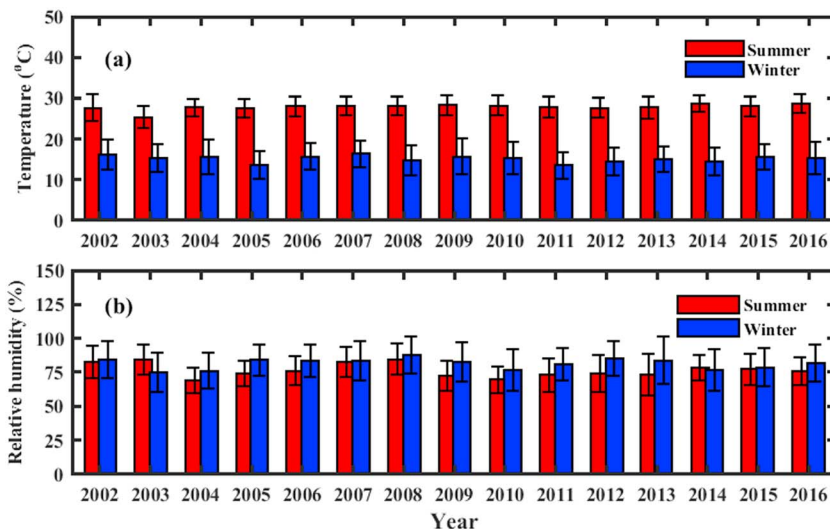


**Figure 17.** Annual variations of ground (a) temperature and (b) relative humidity measured from National Central University-Joss-Waldvogel disdrometer collocated automatic weather station for summer and winter seasons.

represented by red star dotted line in Figures 15a and 15b, respectively. The red star dotted line in Figures 15c and 15d, respectively, denotes the mean reflectivity profile of summer convective rainfall and winter convective rainfall. Also, the mean reflectivity profile of summer stratiform rainfall and winter stratiform rainfall is designated with red star dotted line in Figures 15e and 15f, respectively. As the radar reflectivity is proportional to the sixth power of the drop diameter (Houze, 1993), the larger the particle size, the greater will be the reflectivity. If we look at CFADs of summer and winter, both below and above the melting layer, mean reflectivity profile of summer (red star line in Figure 15a) is higher than the mean reflectivity profile of both seasons (white star dotted line in Figure 15a). On the other hand, mean reflectivity profile of winter (red star line in Figure 15b) is lower than the mean reflectivity profile of both seasons (white star dotted line in Figure 15b). The above characteristics still persist even after separating the summer and winter rainfall into stratiform and convective regimes (Figures 15c–15f). This clearly indicates that relatively large size particles are present at higher levels of summer clouds and are established by higher cloud effective radii values of ice and liquid particles (Figures 16a and 16b). These cloud effective radii values are considered for the disdrometer site (24°–25.2°N and 121°–121.9°E). From Figure 16 it is apparent that the winter has more number of cloud droplets (Figure 16c) of smaller size than summer. The variation of CDNC in summer and winter is alike to that of the Mace and Avey (2017) with higher CDNC in winter than summer. Deep STHs with strong convection in summer (Figures 14 and 13) signify that the summer rainfall is mostly associated with ice or mixed phase clouds, whereas lower storm and melting layers heights in winter specify that winter rainfall typically occurs from liquid water clouds (Wang, 2013). Riming process above the melting layer and enhanced collision-coalescence and accretion below the melting layer are the dominant processes responsible for the particle with a larger size in summer than winter rainfall (Houze, 1993; Hu & Srivastava, 1995). In the case of winter rainfall, because of lower STHs/melting layer heights (~3.5 km in Figure 15b) with least updrafts and downdrafts, the particles do not have the sufficient time to grow to the bigger size as that of the summer rainfall, causing smaller size particle than summer rainfall. In summer, drier conditions on the ground (Figure 17) make the raindrops to reduce their size before reaching the ground by evaporation/breakup, resulting in a decrease of mean reflectivity from 2 to 1 km in summer (Figure 15a). Even though the mean reflectivity profile of summer decrease from 2 to 1 km (Figure 15a), its value is comparatively higher than the mean reflectivity profile of both seasons (white star dotted line in Figure 15a). The above-mentioned processes are the potential causes for the raindrops of bigger size to reach the ground in summer than winter.

## 5. Summary and Conclusions

In the present paper, the RSD characteristics of summer and winter precipitation of north Taiwan have been analyzed by using long-term (~12 years of) RSD spectra from JWD deployed at NCU. Along with the JWD, radar reflectivity mosaic from six ground-based radars, temperature, and relative humidity values from the in situ AWS, ERA-Interim data, as well as data sets from remote sensing instruments (TRMM and MODIS) are used to understand the conceivable reasons for the RSD variations between the two seasons. The chief inferences drawn from the present study are as follows:

1. Mean raindrop concentration of summer and winter clearly shows a demarcation with dominant smaller drops in winter and midsize and larger drops in summer.
2. RSD stratified on the basis of rain rate shows distinct demarcations in small, midsize, and large drops between summer and winter rainfall.
3. Diurnal variation of RSD shows higher mass-weighted mean diameter ($D_m$) and lower normalized intercept ($\log_{10}N_w$) parameters in summer than winter.
4. Classification of summer and winter rainfall into stratiform and convective regimes also shows similar behavior with more small drops in winter and midsize and large drops in summer.
5. Distinct variations in radar reflectivity-rain rate ($Z$-$R$) relations and $\mu$-$\Lambda$ relations are noticed between summer and winter.
6. Clear demarcations in CAPE, water vapor, STH, BBH, vertical profile of radar reflectivity, and CER values of summer and winter seasons are observed.

The winter precipitation over north Taiwan showed narrow raindrop spectra for midsize and large drops with lower shape and slope parameter values than summer precipitation. The statistical Student's *t* test performed to rain integral parameters of summer and winter disproved the null hypothesis and confirms that the

summer RSDs are different from that of the winter. By using a percentage parameter for raindrop concentration (equations (12)–(15)), clear demarcation in drop concentration between summer and winter precipitation is noticed. Summer and winter rainfall are classified into stratiform and convective type by adopting Bringi et al. (2003) classification criteria. Comparison of current results with Bringi et al. (2003) maritime-like and continental-like clusters shows that the mean $D_m$ and $\log_{10}N_w$ values of Taiwan for summer convective rainfall are similar to that of maritime-like cluster, and for the winter convective rainfall are smaller than the both (maritime-like and continental-like) clusters. The $Z$-$R$ relations deduced in the present study are found to be different from that of the currently adopting $Z$-$R$ relations in Taiwan QPE. This clearly designates that there is prerequisite to implement updated $Z$-$R$ relations in the estimation of Taiwan rainfall by QPE.

As this study is carried out by using long-term observational data, these results can be useful in improving the QPE from radars as well as in cloud microphysics parameterization.

## References

Amburn, S. A., & Wolf, P. L. (1997). VIL density as a hail indicator. *Weather and Forecasting*, *12*(3), 473–478. https://doi.org/10.1175/1520-0434(1997)012<0473:VDAAHI>2.0.CO;2

Angulo-Martinez, M., & Barros, A. P. (2015). Measurement uncertainty in rainfall kinetic energy and intensity relationships for soil erosion studies: An evaluation using PARSIVEL disdrometers in the Southern Appalanchian Mountains. *Geomorphology*, *228*, 28–40. https://doi.org/10.1016/j.geomorph.2014.07.036

Atlas, D., & Ulbrich, C. (2006). Drop size spectra and integral remote sensing parameters in the transition from convective to stratiform rain. *Geophysical Research Letters*, *33*, L16803. https://doi.org/10.1029/2006GL026824

Atlas, D., Ulbrich, C. W., Marks, F. D. Jr., Amitai, E., & Williams, C. R. (1999). Systematic variation of drop size and radar-rainfall relations. *Journal of Geophysical Research*, *104*(D6), 6155–6169. https://doi.org/10.1029/1998JD200098

Atlas, D., & Williams, C. R. (2003). The anatomy of a continental tropical convective storm. *Journal of the Atmospheric Sciences*, *60*(1), 3–15. https://doi.org/10.1175/1520-0469(2003)060%3C0003:TAOACT%3E2.0.CO;2

Awaka, J., Iguchi, T., Kumagai, H., & Okamoto, K. (1997). Rain type classification algorithm for TRMM precipitation radar. *In Proc. 1997 Int. Geoscience and Remote Sensing Symposium* (pp. 1633–1635). Singapore: IEEE.

Awaka, J., Iguchi, T., & Okomoto, K. (2009). TRMM PR standard algorithm 2A23 and its performance on bright band detection. *Journal of the Meteorological Society of Japan*, *87A*(A), 31–52. https://doi.org/10.2151/jmsj.87A.31

Badron, K., Ismail, A. F., Din, J., & Tharek, A. R. (2011). Rain induced attenuation studies for V-band satellite communication in tropical region. *Journal of Atmospheric and Solar - Terrestrial Physics*, *73*(5–6), 601–610. https://doi.org/10.1016/j.jastp.2010.12.006

Bennartz, R. (2007). Global assessment of marine boundary layer cloud droplet number concentration from satellite. *Journal of Geophysical Research*, *112*, D02201. https://doi.org/10.1029/2006JD007547

Bennartz, R., & Rausch, J. (2017). Global and regional estimates of warm cloud droplet number concentration based on 13 years of AQUA-MODIS observations. *Atmospheric Chemistry and Physics*, *17*(16), 9815–9836. https://doi.org/10.5194/acp-17-9815-2017

Boodoo, S., Hudak, D., Ryzhkov, A., Zhang, P., Donaldson, N., Sills, D., & Reid, J. (2015). Quantitative precipitation estimation from a C-band dual-polarized radar for the 8 July 013 flood in Toronto, Canada. *Journal of Hydrometeorology*, *16*(5), 2027–2044. https://doi.org/10.1175/JHM-D-15-0003.1

Brandes, E. A., Zhang, G., & Vivekanandan, J. (2002). Experiments in rainfall estimation with a polarimetric radar in a subtropical environment. *Journal of Applied Meteorology*, *41*(6), 674–685. https://doi.org/10.1175/1520-0450(2002)041<0674:EIREWA>2.0.CO;2

Brandes, E. A., Zhang, G., & Vivekanandan, J. (2003). An evaluation of a drop distribution–based rainfall estimator. *Journal of Applied Meteorology*, *42*(5), 652–660. https://doi.org/10.1175/1520-0450(2003)042,0652:AEOADD.2.0.CO;2

Brenguier, J. L., Burnet, F., & Geoffroy, O. (2011). Cloud optical thickness and liquid water path—Does the $k$ coefficient vary with droplet concentration? *Atmospheric Chemistry and Physics*, *11*(18), 9771–9786. https://doi.org/10.5194/acp-11-9771-2011

Brenguier, J. L., Pawlowska, H., Schuller, L., Preusker, R., Fischer, J., & Fouquart, Y. (2000). Radiative properties of boundary layer clouds, droplet effective radius versus number concentration. *Journal of the Atmospheric Sciences*, *57*(6), 803–821. https://doi.org/10.1175/1520-0469(2000)057<0803:rpoblc>2.0.co;2

Bringi, V., Chandrasekar, V., Hubbert, J., Gorgucci, E., Randeu, W. L., & Schoenhuber, M. (2003). Raindrop size distribution in different climatic regimes from disdrometer and dual-polarized radar analysis. *Journal of the Atmospheric Sciences*, *60*(2), 354–365. https://doi.org/10.1175/1520-0469(2003)060%3C0354:RSDIDC%3E2.0.CO;2

Campos, E., & Zawadzki, I. (2000). Instrumental uncertainties in Z-R relations. *Journal of Applied Meteorology*, *39*(7), 1088–1102. https://doi.org/10.1175/1520-0450(2000)039<1088:IUIZRR>2.0.CO;2

Campos, E. F., Zawadzki, I., Petitdidier, M., & Fernandez, M. (2006). Measurement of raindrop size distributions in tropical rain at Costa Rica. *Journal of Hydrology*, *328*(1-2), 98–109. https://doi.org/10.1016/j.jhydrol.2005.11.047

Cao, Q., Zhang, G., Brandes, E., Schuur, T., Ryzhkov, A., & Ikeda, K. (2008). Analysis of video disdrometer and polarimetric radar to characterize rain microphysics in Oklahoma. *Journal of Applied Meteorology and Climatology*, *47*(8), 2238–2255. https://doi.org/10.1175/2008JAMC1732.1

Chakravarty, K., & Maitra, A. (2010). Rain attenuation studies over an earth space path at a tropical location. *Journal of Atmospheric and Solar - Terrestrial Physics*, *72*(1), 135–138. https://doi.org/10.1016/j.jastp.2009.10.018

Chakravarty, K., & Raj, P. E. (2013). Raindrop size distributions and their association with characteristics of clouds and precipitation during monsoon and post-monsoon periods over a tropical Indian station. *Atmospheric Research*, *124*, 181–189. https://doi.org/10.1016/j.atmosres.2013.01.005

Chakravarty, K., Raj, P. E., Bhattacharya, A., & Maitra, A. (2013). Microphysical characteristics of clouds and precipitation during pre-monsoon and monsoon period over a tropical Indian station. *Journal of Atmospheric and Solar - Terrestrial Physics*, *94*, 28–33. https://doi.org/10.1016/j.jastp.2012.12.016

Chang, P.-L., Lin, P.-F., Jou, B. J.-D., & Zhang, J. (2009). An application of reflectivity climatology in constructing radar hybrid scans over complex terrain. *Journal of Atmospheric and Oceanic Technology*, *26*(7), 1315–1327. https://doi.org/10.1175/2009JTECHA1162.1

Chang, W.-Y., Wang, T.-C. C., & Lin, P.-L. (2009). Characteristics of the raindrop size distribution and drop shape relation in typhoon systems in the western Pacific from the 2D video disdrometer and NCU C-band polarimetric radar. *Journal of Atmospheric and Oceanic Technology*, *26*(10), 1973–1993. https://doi.org/10.1175/2009JTECHA1236.1

Chen, B., Hu, Z., Liu, L., & Zhang, G. (2017). Raindrop size distribution measurements at 4,500 m on the Tibetan Plateau during TIPEX-III. *Journal of Geophysical Research: Atmospheres*, *122*, 11,092–11,106. https://doi.org/10.1002/2017JD027233

Chen, B., Wang, J., & Gong, D. (2016). Raindrop size distribution in a midlatitude continental squall line measured by Thies optical disdrometers over East China. *Journal of Applied Meteorology and Climatology*, *55*(3), 621–634. https://doi.org/10.1175/JAMC-D-15-0127.1

Chen, B., Wang, Y., & Ming, J. (2012). Microphysical characteristics of the raindrop size distribution in Typhoon Morakot (2009). *Journal of Tropical Meteorology*, *18*, 162–171. https://doi.org/10.3969/j.issn.1006-8775.2012.02.006

Chen, B., Yang, J., & Pu, J. (2013). Statistical characteristics of raindrop size distribution in the Meiyu season observed in eastern China. *Journal of the Meteorological Society of Japan*, *91*(2), 215–227. https://doi.org/10.2151/jmsj.2013-208

Chen, C. S., & Chen, Y. L. (2003). The rainfall characteristic of Taiwan. *Monthly Weather Review*, *131*(7), 1323–1341. https://doi.org/10.1175/1520-0493(2003)131%3C1323:TRCOT%3E2.0.CO;2

Chen, S., Hong, Y., Kulie, M., Behrangi, A., Stepanian, P. M., Cao, Q., et al. (2016). Comparison of snowfall estimates from the NASA cloudsat cloud profiling radar and NOAA/NSSL multi radar multi sensor system. *Journal of Hydrology*, *541*, 862–872. https://doi.org/10.1016/j.jhydrol.2016.07.047

Chen, T.-C., Yen, M.-C., Hsieh, J.-C., & Arritt, R. W. (1999). Preliminary results of the rainfall measured by the automatic rainfall and meteorological telemetry system in Taiwan: Diurnal and seasonal variations. *Bulletin of the American Meteorological Society*, *80*(11), 2299–2312. https://doi.org/10.1175/1520-0477(1999)080<2299:DASVOT>2.0.CO;2

Chu, Y.-H., & Su, C.-L. (2008). An investigation of the slope-shape relation for gamma raindrop size distribution. *Journal of Applied Meteorology and Climatology*, *47*(10), 2531–2544. https://doi.org/10.1175/2008JAMC1755.1

Cohen, C., & McCaul, E. W. Jr. (2006). The sensitivity of simulated convective storms to variations in prescribed single-moment microphysics parameters that describe particle distributions, sizes, and numbers. *Monthly Weather Review*, *134*(9), 2547–2565. https://doi.org/10.1175/MWR3195.1

Das, S. K., Konwar, M., Chakravarty, K., & Deshpande, S. M. (2017). Raindrop size distribution of different cloud types over the Western Ghats using simultaneous measurements from micro-rain radar and disdrometer. *Atmospheric Research*, *186*(2017), 72–82. https://doi.org/10.1016/j.atmosres.2016.11.003

Dee, D. P., Uppala, S. M., Simmons, A. J., Berrisford, P., Poli, P., Kobayashi, S., et al. (2011). The ERA-interim reanalysis: Configuration and performance of the data assimilation system. *Quarterly Journal of the Royal Meteorological Society*, *137*(656), 553–597. https://doi.org/10.1002/qj.828

Deo, A., & Walsh, K. J. E. (2016). Contrasting tropical cyclone and non-tropical cyclone related rainfall drop size distribution at Darwin, Australia. *Atmospheric Research*, *181*, 81–94. https://doi.org/10.1016/j.atmosres.2016.06.015

Fadnavis, S., Deshpande, M., Ghude, S. D., & Raj, P. E. (2014). Simulation of severe thunder storm event: A case study over Pune, India. *Natural Hazards*, *72*(2), 927–943. https://doi.org/10.1007/s11069-014-1047-1

Gilmore, M. S., Straka, J. M., & Rasmussen, E. N. (2004). Precipitation uncertainty due to variations in precipitation particle parameters with in a simple microphysics scheme. *Monthly Weather Review*, *132*(11), 2610–2627. https://doi.org/10.1175/MWR2810.1

Gunn, R., & Kinzer, G. D. (1949). The terminal velocity of fall for water droplets in stagnant air. *Journal of Meteorology*, *6*(4), 243–248. https://doi.org/10.1175/1520-0469(1949)006<0243:TTVOFF>2.0.CO;2

Heymsfield, A. J., Bansemer, A., Field, P. R., Durden, S. L., Stith, J. L., Dye, J. E., et al. (2002). Observations and parameterizations of particle size distributions in deep tropical cirrus and stratiform precipitating clouds: Results from in situ observations in TRMM field campaigns. *Journal of Atmospheric Science*, *59*(24), 3457–3491. https://doi.org/10.1175/1520-0469(2002)059<3457:OAPOPS>2.0.CO;2

Hou, A. Y., Skofronick-Jackson, G., Kummerow, C. D., & Shepherd, J. M. (2008). Global precipitation measurement. In S. Michaelides (Ed.), *Precipitation: Advances in measurement, estimation and prediction* (pp. 131–169). New York: Springer. https://doi.org/10.1007/978-3-540-77655-0_6

Houze, R. A. Jr. (1993). *Cloud dynamics*. San Diego, CA: Academic Press Inc.

Hu, Z., & Srivastava, R. C. (1995). Evolution of raindrop size distribution by coalescence, breakup, and evaporation: Theory and observation. *Journal of the Atmospheric Sciences*, *52*(10), 1761–1783. https://doi.org/10.1175/1520-0469(1995)052<1761:EORSDB>2.0.CO;2

Iguchi, T., Kozu, T., Meneghini, R., Awaka, J., & Okamoto, K. (2000). Rain-profiling algorithm for the TRMM precipitation radar. *Journal of Applied Meteorology*, *39*(12), 2038–2052. https://doi.org/10.1175/1520-0450(2001)040%3C2038:RPAFTT%3E2.0.CO;2

Janapati, J., Seela, B. K., Reddy, M. V., Reddy, K. K., Lin, P.-L., Rao, T. N., & Liu, C.-Y. (2017). A study on raindrop size distribution variability in before and after landfall precipitations of tropical cyclones observed over southern India. *Journal of Atmospheric and Solar - Terrestrial Physics*, *159*, 23–40. https://doi.org/10.1016/j.jastp.2017.04.011

Jayalakshmi, J., & Reddy, K. K. (2014). Raindrop size distributions of southwest and northeast monsoon heavy precipitations observed over Kadapa (14°40N, 78°820E), a semi-arid region of India. *Current Science*, *107*(8), 1312–1320.

Joss, J., & Waldvogel, A. (1969). Raindrop size distribution and sampling size errors. *Journal of the Atmospheric Sciences*, *26*(3), 566–569. https://doi.org/10.1175/1520-0469(1969)026%3C0566:RSDASS%3E2.0.CO;2

Jung, S. A., Lee, D.-I., Jou, B. J.-D., & Uyeda, H. (2012). Microphysical properties of maritime squall line observed on June 2, 2008 in Taiwan. *Journal of the Meteorological Society of Japan*, *90*(5), 833–850. https://doi.org/10.2151/jmsj.2012-516

King, M. D., Menzel, W. P., Kaufman, Y. J., Tanre, D., Gao, B.-C., Platnick, S., et al. (2003). Cloud and aerosol properties, precipitable water, and profiles of temperature and water vapor. *IEEE Transactions on Geoscience and Remote Sensing*, *41*(2), 442–458. https://doi.org/10.1109/TGRS.2002.808226

Kozu, T., Iguchi, T., Kubota, T., Yoshida, N., Seto, S., Kwiatkowski, J., & Takayabu, Y. N. (2009). Feasibility of raindrop size distribution parameter estimation with TRMM precipitation radar observations of shallow convection with a rain cell model. *Journal of the Meteorological Society of Japan*, *87A*, 53–66. https://doi.org/10.2151/jmsj.87A.53

Kozu, T., Reddy, K. K., Mori, S., Thurai, M., Ong, J. T., & Rao, D. N. (2006). Seasonal and diurnal variations of raindrop size distribution in Asian monsoon region. *Journal of the Meteorological Society of Japan*, *84A*, 195–209. https://doi.org/10.2151/jmsj.84A.195

Kozu, T., Shimomai, T., & Kashiwagi, N. (2009). Raindrop size distribution modeling from a statistical rain parameter relation and its application to the TRMM precipitation radar rain retrieval algorithm. *Journal of Applied Meteorology and Climatology*, *48*(4), 716–724. https://doi.org/10.1175/2008JAMC1998.1

Krishna, U. V. M., Reddy, K. K., Seela, B. K., Shirooka, R., Lin, P.-L., & Pan, C.-J. (2016). Raindrop size distribution of easterly and westerly monsoon precipitation observed over Palau islands in the Western Pacific Ocean. *Atmospheric Research*, *174-175*, 41–51. https://doi.org/10.1016/j.atmosres.2016.01.013

Kumar, L. S., Lee, Y. H., & Ong, J. T. (2010). Truncated gamma drop size distribution models for rain attenuation in Singapore. *IEEE Transactions on Antennas and Propagation*, *58*(4), 1325–1335. https://doi.org/10.1109/TAP.2010.2042027

Kumar, L. S., Lee, Y. H., & Ong, J. T. (2011). Two-parameter gamma drop size distribution models for Singapore. *IEEE Transactions on Geoscience and Remote Sensing*, *49*(9), 3371–3380. https://doi.org/10.1109/TGRS.2011.2124464

Kumar, S. B., & Reddy, K. K. (2013). Raindrop size distribution characteristics of cyclonic and north east monsoon thunderstorm precipitating clouds observed over Kadapa (14.47°N, 78.82°E), tropical semi-arid region of India. *Mausam*, *64*(1), 35–48.

Kumari, N. P. A., Kumar, S. B., Jayalakshmi, J., & Reddy, K. K. (2014). Raindrop size distribution variations in JAL and NILAM cyclones induced precipitation observed over Kadapa (14.47°N, 78.82°E), a tropical semi-arid region of India. *Indian Journal of Radio & Space Physics*, *43*, 57–66. http://nopr.niscair.res.in/handle/123456789/27164

Kummerow, C., Hong, Y., Olson, W. S., Yang, S., Adler, R. F., McCollum, J., & Wilheit, T. T. (2001). The evolution of the Goddard profile algorithm (GPROF) for rainfall estimation from passive microwave sensors. *Journal of Applied Meteorology*, *40*(11), 1801–1820. https://doi.org/10.1175/1520-0450(2001)040%3C1801:TEOTGP%3E2.0.CO;2

Lam, H. Y., Din, J., & Jong, S. L. (2015). Statistical and physical descriptions of raindrop size distributions in equatorial Malaysia from disdrometer observations. *Advances in Meteorology*, *2015*, 1–14. https://doi.org/10.1155/2015/253730

Lee, G., & Zawadzki, I. (2005). Variability of drop size distributions: Noise and noise filtering in disdrometric data. *Journal of Applied Meteorology*, *44*(5), 634–652. https://doi.org/10.1175/JAM2222.1

Liao, L., Meneghini, R., & Tokay, A. (2014). Uncertainties of GPM DPR rain estimates caused by DSD parameterizations. *Journal of Applied Meteorology and Climatology*, *53*(11), 2524–2537. https://doi.org/10.1175/JAMC-D-14-0003.1

Mace, G. G., & Avey, S. (2017). Seasonal variability of warm boundary layer cloud and precipitation properties in the Southern Ocean as diagnosed from A-Train data. *Journal of Geophysical Research: Atmospheres*, *122*, 1015–1032. https://doi.org/10.1002/2016JD025348

Maki, M., Keenan, T. D., Sasaki, Y., & Nakamura, K. (2001). Characteristics of the raindrop size distribution in tropical continental squall lines observed in Darwin, Australia. *Journal of Applied Meteorology*, *40*(8), 1393–1412. https://doi.org/10.1175/1520-0450(2001)040<1393:COTRSD>2.0.CO;2

Martin, G. M., Johnson, D. W., & Spice, A. (1994). The measurement and parameterization of effective radius of droplets in warm stratocumulus clouds. *Journal of the Atmospheric Sciences*, *51*(13), 1823–1842. https://doi.org/10.1175/1520-0469(1994)051<1823:TMAPOE>2.0.CO;2

Marzuki, M., Kozu, T., Shimomai, T., Randeu, W. L., Hashiguchi, H., & Shibagaki, Y. (2009). Diurnal variation of rain attenuation obtained from measurement of raindrop size distribution in equatorial Indonesia. *IEEE Transactions on Antennas and Propagation*, *57*(4), 1191–1196. https://doi.org/10.1109/TAP.2009.2015812

Marzuki, Randeu, W. L., Kozu, T., Shimomai, T., Hashiguchi, H., & Schönhuber, M. (2013). Raindrop axis ratios, fall velocities and size distribution over Sumatra from 2D-video disdrometer measurement. *Atmospheric Research*, *119*, 23–37. https://doi.org/10.1016/j.atmosres.2011.08.006

McFarquhar, G. M., Hsieh, T.-L., Freer, M., Mascio, J., & Jewett, B. F. (2015). The characterization of ice hydrometeor gamma size distributions as volumes in $N_0$–$\lambda$–$\mu$ phase space: Implications for microphysical process modeling. *Journal of the Atmospheric Sciences*, *72*(2), 892–909. https://doi.org/10.1175/JAS-D-14-0011.1

McFarquhar, G. M., & List, R. (1993). The effect of curve fits for the disdrometer calibration on raindrop spectra, rainfall rate and radar reflectivity. *Journal of Applied Meteorology*, *32*(4), 774–782. https://doi.org/10.1175/1520-0450(1993)032%3C0774:TEOCFF%3E2.0.CO;2

Nakajima, T., & King, M. D. (1990). Determination of the optical thickness and effective particle radius of clouds from reflected solar radiation measurements, Part I: Theory. *Journal of the Atmospheric Sciences*, *47*(15), 1878–1893. https://doi.org/10.1175/1520-0469(1990)047%3C1878:DOTOTA%3E2.0.CO;2

Nakamura, K., & Iguchi, T. (2007). Dual-wavelength radar algorithm. In V. Levizzani, P. Bauer, & F. J. Turk (Eds.), *Measuring precipitation from space* (pp. 225–234). New York: Springer. https://doi.org/10.1007/978-1-4020-5835-6_18

Nanko, K., Moskalski, S. M., & Torres, R. (2016). Rainfall erosivity–intensity relationships for normal rainfall events and a tropical cyclone on the US southeast coast. *Journal of Hydrology*, *534*, 440–450. https://doi.org/10.1016/j.jhydrol.2016.01.022

Niu, S., Jia, X., Sang, J., Liu, X., Lu, C., & Liu, Y. (2010). Distributions of raindrop sizes and fall velocities in a semiarid plateau climate: Convective versus stratiform rains. *Journal of Applied Meteorology and Climatology*, *49*(4), 632–645. https://doi.org/10.1175/2009JAMC2208.1

Pawlowska, H., & Brenguier, J.-L. (2003). An observational study of drizzle formation in stratocumulus clouds for general circulation models. *Journal of Geophysical Research*, *108*(D15), 8630. https://doi.org/10.1029/2002JD002679

Platnick, S., King, M. D., Ackerman, S. A., Menzel, W. P., Baum, B. A., Riedl, J. C., & Frey, R. A. (2003). The MODIS cloud products: Algorithms and examples from Terra. *IEEE Transactions on Geoscience and Remote Sensing*, *41*(2), 459–473. https://doi.org/10.1109/TGRS.2002.808301

Platnick, S., et al. (2015). MODIS atmosphere L3 daily product. NASA MODS Adaptive Processing System, Goddard Space Flight Center. https://doi.org/10.5067/MODIS/MOD08_D3.006

Radhakrishna, B., & Rao, T. N. (2010). Differences in cyclonic raindrop size distribution from south-west to north-east monsoon season and from that of non-cyclonic rain. *Journal of Geophysical Research*, *115*, D16205. https://doi.org/10.1029/2009JD013355

Rao, T. N., Radhakrishna, B., Nakamura, K., & Rao, N. P. (2009). Differences in raindrop size distribution from southwest monsoon to northeast monsoon at Gadanki. *Quarterly Journal of the Royal Meteorological Society*, *135*(643), 1630–1637. https://doi.org/10.1002/qj.432

Reddy, K. K., & Kozu, T. (2003). Measurements of raindrop size distribution over Gadanki during southwest and northeast monsoon. *Indian Journal of Radio & Space Physics*, *32*, 286–295. http://nopr.niscair.res.in/handle/123456789/25807

Remer, L. A., Kaufman, Y. J., Tanré, D., Mattoo, S., Chu, D. A., Martins, J. V., et al. (2005). The MODIS aerosol algorithm, products and validation. *Journal of the Atmospheric Sciences*, *62*(4), 947–973. https://doi.org/10.1175/JAS3385.1

Rosenfeld, D., & Ulbrich, C. W. (2003). Cloud microphysical properties, processes, and rainfall estimation opportunities. *Meteorological Monographs*, *30*(52), 237–258. https://doi.org/10.1175/0065-9401(2003)030%3C0237:CMPPAR%3E2.0.CO;2

Rosewell, C. J. (1986). Rainfall kinetic energy in eastern Australia. *Journal of Climate and Applied Meteorology*, *25*(11), 1695–1701. https://doi.org/10.1175/1520-0450(1986)025%3C1695:RKEIEA%3E2.0.CO;2

Ryzhkov, A. V., & Zrnic, D. S. (1995). Comparison of dual polarization radar estimators of rain. *Journal of Atmospheric and Oceanic Technology*, *12*(2), 249–256. https://doi.org/10.1175/1520-0426(1995)012%3C0249:CODPRE%3E2.0.CO;2

Sauvageot, H., & Lacaux, J. P. (1995). The shape of averaged drop size *distributions*. *Journal of the Atmospheric Sciences*, *52*(8), 1070–1083. https://doi.org/10.1175/1520-0469(1995)052%3C1070:TSOADS%3E2.0.CO;2

Seela, B. K., Janapati, J., Lin, P.-L., Reddy, K. K., Shirooka, R., & Wang, P. K. (2017). A comparison study of summer season raindrop size distribution between Palau and Taiwan, two islands in western Pacific. *Journal of Geophysical Research: Atmospheres*, *122*, 11,787–11,805. https://doi.org/10.1002/2017JD026816

Seliga, T. A., & Bringi, V. N. (1976). Potential use of the radar differential reflectivity measurements at orthogonal polarizations for measuring precipitation. *Journal of Applied Meteorology*, *15*(1), 69–76. https://doi.org/10.1175/1520-0450(1976)015%3C0069:PUORDR%3E2.0.CO;2

Sheppard, B. E. (1990). Effect of irregularities in the diameter classification of raindrops by the Joss–Waldvogel disdrometer. *Journal of Atmospheric and Oceanic Technology*, *7*(1), 180–183. https://doi.org/10.1175/1520-0426(1990)007%3C0180:EOIITD%3E2.0.CO;2

Sheppard, B. E., & Joe, P. I. (1994). Comparison of raindrop size distribution measurements by a Joss-Waldvogel disdrometer, a PMS 2DG spectrometer, and a POSS Doppler radar. *Journal of Atmospheric and Oceanic Technology*, *11*(4), 874–887. https://doi.org/10.1175/1520-0426(1994)011%3C0874:CORSDM%3E2.0.CO;2

Smith, J. A., Hui, E., Steiner, M., Baeck, M. L., Krajewski, W. F., & Ntelekos, A. A. (2009). Variability of rainfall rate and raindrop size distributions in heavy rain. *Water Resources Research*, *45*, W04430. https://doi.org/10.1029/2008WR006840

Sreekanth, T. S., Varikoden, H., Sukumar, N., & Kumar, G. M. (2017). Microphysical characteristics of rainfall during different seasons over a coastal tropical station using disdrometer. *Hydrological Processes*, *31*(14), 2556–2565. https://doi.org/10.1002/hyp.11202

Steiner, M., Houze, R. A., & Yuter, S. E. (1995). Climatological characterization of 3-dimensional storm structure from operational radar and rain-gauge data. *Journal of Applied Meteorology*, *34*(9), 1978–2007. https://doi.org/10.1175/1520-0450(1995)034%3C1978:CCOTDS%3E2.0.CO;2

Steiner, M., Smith, J. A., & Uijlenhoet, R. (2004). A microphysical interpretation of radar reflectivity-rain rate relationships. *Journal of the Atmospheric Sciences*, *61*(10), 1114–1131. https://doi.org/10.1175/1520-0469(2004)061%3C1114:AMIORR%3E2.0.CO;2

Suh, S.-H., You, C.-H., & Lee, D.-I. (2016). Climatological characteristics of raindrop size distributions in Busan, Republic of Korea. *Hydrology and Earth System Sciences*, *20*(1), 193–207. https://doi.org/10.5194/hess-20-193-2016

Tang, Q., Xiao, H., Guo, C., & Feng, L. (2014). Characteristics of the raindrop size distributions and their retrieved polarimetric radar parameters in northern and southern China. *Atmospheric Research*, *135-136*, 59–75. https://doi.org/10.1016/j.atmosres.2013.08.003

Tapiador, F. J., Haddad, Z. S., & Turk, J. (2014). A probabilistic view on raindrop size distribution modeling: A physical interpretation of rain microphysics. *Journal of Hydrometeorology*, *15*(1), 427–443. https://doi.org/10.1175/JHM-D-13-033.1

Thurai, M., Gatlin, P. N., & Bringi, V. N. (2016). Separating stratiform and convective rain types based on the drop size distribution characteristics using 2D video disdrometer data. *Atmospheric Research*, *169*, 416–423. https://doi.org/10.1016/j.atmosres.2015.04.011

Tokay, A., Bashor, P. G., Habib, E., & Kasparis, T. (2008). Raindrop size distribution measurements in tropical cyclones. *Monthly Weather Review*, *136*(5), 1669–1685. https://doi.org/10.1175/2007MWR2122.1

Tokay, A., Kruger, A., & Krajewski, W. F. (2001). Comparison of drop size distribution measurements by impact and optical disdrometers. *Journal of Applied Meteorology*, *40*(11), 2083–2097. https://doi.org/10.1175/1520-0450(2001)040%3C2083:CODSDM%3E2.0.CO;2

Tokay, A., Petersen, W. A., Gatlin, P., & Wingo, M. (2013). Comparison of raindrop size distribution measurements by collocated disdrometers. *Journal of Atmospheric and Oceanic Technology*, *30*(8), 1672–1690. https://doi.org/10.1175/JTECH-D-12-00163.1

Tokay, A., & Short, D. A. (1996). Evidence from tropical raindrop spectra of the origin of rain from stratiform versus convective clouds. *Journal of Applied Meteorology*, *35*(3), 355–371. https://doi.org/10.1175/1520-0450(1996)035%3C0355:EFTRSO%3E2.0.CO;2

Tokay, A., Short, D. A., Williams, C. R., Ecklund, W. L., & Gage, K. S. (1999). Tropical rainfall associated with convective and stratiform clouds: Intercomparison of disdrometer and profiler measurements. *Journal of Applied Meteorology*, *38*(3), 302–320. https://doi.org/10.1175/1520-0450(1999)038<0302:TRAWCA>2.0.CO;2

Ulbrich, C. W. (1983). Natural variations in the analytical form of the raindrop size distribution. *Journal of Climate and Applied Meteorology*, *22*(10), 1764–1775. https://doi.org/10.1175/1520-0450(1983)022%3C1764:NVITAF%3E2.0.CO;2

Ulbrich, C. W., & Atlas, D. (2007). Microphysics of raindrop size spectra: Tropical continental and maritime storms. *Journal of Applied Meteorology and Climatology*, *46*(11), 1777–1791. https://doi.org/10.1175/2007JAMC1649.1

Vivekanandan, J., Zhang, G., & Brandes, E. (2004). Polarimetric radar estimators based on a constrained gamma drop size distribution model. *Journal of Applied Meteorology*, *43*(2), 217–230. https://doi.org/10.1175/1520-0450(2004)043<0217:PREBOA>2.0.CO;2

Wainwright, C. E., Dawson, D. T. II, Xue, M., & Zhang, G. (2014). Diagnosing the intercept parameters of the exponential drop size distributions in a single-moment microphysics scheme and impact on supercell storm simulations. *Journal of Applied Meteorology and Climatology*, *53*(8), 2072–2090. https://doi.org/10.1175/JAMC-D-13-0251.1

Waldvogel, A. (1974). The $N_0$ jump of raindrop spectra. *Journal of the Atmospheric Sciences*, *31*(4), 1067–1078. https://doi.org/10.1175/1520-0469(1974)031<1067:TJORS>2.0.CO;2

Wang, P. K. (2013). *Physics and dynamics of clouds and precipitation* (p. 467). New York: Cambridge University Press. https://doi.org/10.1017/CBO9780511794285

Wen, G., Xiao, H., Yang, H., Bi, Y., & Xu, W. (2017). Characteristics of summer and winter precipitation over northern China. *Atmospheric Research*, *197*, 390–406. https://doi.org/10.1016/j.atmosres.2017.07.023

Wen, J., Zhao, K., Huang, H., Zhou, B., Yang, Z., Chen, G., & Lee, W.-C. (2017). Evolution of microphysical structure of a subtropical squall line observed by a polarimetric radar and a disdrometer during OPACC in eastern China. *Journal of Geophysical Research: Atmospheres*, *122*, 8033–8050. https://doi.org/10.1002/2016JD026346

Yang, L.-G. (2000). Analysis of afternoon convective precipitation over Taiwan (in Chinese). M.S. thesis, Institute of Atmospheric Physics, National Central University, Taiwan, 120 pp. (Available from Institute of Atmospheric Physics, National Central University, Chung-Li, Taiwan.)

Yen, M.-C., & Chen, T.-C. (2002). A revisit of the east-Asian cold surges. *Journal of the Meteorological Society of Japan*, *80*(5), 1115–1128. https://doi.org/10.2151/jmsj.80.1115

Yuter, S. E., & Houze, R. A. Jr. (1995). Three-dimensional kinematic and microphysical evolution of Florida cumulonimbus. Part II: Frequency distributions of vertical velocity, reflectivity, and differential reflectivity. *Monthly Weather Review*, *123*(7), 1941–1963. https://doi.org/10.1175/1520-0493(1995)123<1941:TDKAME>2.0.CO;2

Zeng, S., Riedi, J., Trepte, C. R., Winker, D. M., & Hu, Y.-X. (2014). Study of global cloud droplet number concentration with A-Train satellites. *Atmospheric Chemistry and Physics*, *14*(14), 7125–7134. https://doi.org/10.5194/acp-14-7125-2014

Zhang, G., Vivekanandan, J., Brandes, E. A., Meneghini, R., & Kozu, T. (2003). The shape slope relation in observed gamma raindrop size distributions: Statistical error or useful information? *Journal of Atmospheric and Oceanic Technology*, *20*(8), 1106–1119. https://doi.org/10.1175/1520-0426(2003)020<1106:TSRIOG>2.0.CO;2

Zhang, J., Howard, K., Chang, P.-L., Chiu, P. T.-K., Chen, C.-R., Langston, C., et al. (2009). High-resolution QPE system for Taiwan. In S. K. Park, & L. Xu (Eds.), *Data assimilation for atmospheric, oceanic and hydrological applications* (pp. 147–162). Berlin: Springer-Verlag. https://doi.org/10.1007/978-3-540-71056-1_7

Zhang, J., Howard, K., & Gourley, J. J. (2005). Constructing three-dimensional multiple-radar reflectivity mosaics: Examples of convective storms and stratiform rain echoes. *Journal of Atmospheric and Oceanic Technology*, *22*(1), 30–42. https://doi.org/10.1175/JTECH-1689.1